Ultrasonics Sonochemistry 93 (2023) 106291

Contents lists available at ScienceDirect

Ultrasonics Sonochemistry

journal homepage: www.elsevier.com/locate/ultson

An optical and acoustic investigation of microbubble cavitation in small channels under therapeutic ultrasound conditions

Xiaoxiao Zhao [a,b,*], Alex Wright [b], David E. Goertz [a,b,*]

[a] Department of Medical Biophysics, University of Toronto, M5G 1L7, Canada
[b] Sunnybrook Research Institute, 2075 Bayview Ave, Toronto M4N 3M5, Canada

ARTICLE INFO

Keywords:
Antivascular ultrasound
Cavitation
Drug delivery
Focused ultrasound
Microbubble
Nanobubble

ABSTRACT

Therapeutic focused ultrasound in combination with encapsulated microbubbles is being widely investigated for its ability to elicit bioeffects in the microvasculature, such as transient permeabilization for drug delivery or at higher pressures to achieve 'antivascular' effects. While it is well established that the behaviors of microbubbles are altered when they are situated within sufficiently small vessels, there is a paucity of data examining how the bubble population dynamics and emissions change as a function of channel (vessel) diameter over a size range relevant to therapeutic ultrasound, particularly at pressures relevant to antivascular ultrasound. Here we use acoustic emissions detection and high-speed microscopy (10 kframes/s) to examine the behavior of a polydisperse clinically employed agent (Definity®) in wall-less channels as their diameters are scaled from 1200 to 15 μm. Pressures are varied from 0.1 to 3 MPa using either a 5 ms pulse or a sequence of 0.1 ms pulses spaced at 1 ms, both of which have been previously employed in an *in vivo* context. With increasing pressure, the 1200 μm channel – on the order of small arteries and veins – exhibited inertial cavitation, 1/2 subharmonics and 3/2 ultraharmonics, consistent with numerous previous reports. The 200 and 100 μm channels – in the size range of larger microvessels less affected by therapeutic focused ultrasound - exhibited a distinctly different behavior, having muted development of 1/2 subharmonics and 3/2 ultraharmonics and reduced persistence. These were associated with radiation forces displacing bubbles to the distal wall and inducing clusters that then rapidly dissipated along with emissions. As the diameter transitioned to 50 and then 15 μm – a size regime that is most relevant to therapeutic focused ultrasound - there was a higher threshold for the onset of inertial cavitation as well as subharmonics and ultraharmonics, which importantly had more complex orders that are not normally reported. Clusters also occurred in these channels (e.g. at 3 MPa, the mean lateral and axial sizes were 23 and 72 μm in the 15 μm channel; 50 and 90 μm in the 50 μm channel), however in this case they occupied the entire lumens and displaced the wall boundaries. Damage to the 15 μm channel was observed for both pulse types, but at a lower pressure for the long pulse. Experiments conducted with a 'nanobubble' (<0.45 μm) subpopulation of Definity followed broadly similar features to 'native' Definity, albeit at a higher pressure threshold for inertial cavitation. These results provide new insights into the behavior of microbubbles in small vessels at higher pressures and have implications for therapeutic focused ultrasound cavitation monitoring and control.

1. Introduction

Therapeutic focused ultrasound (FUS) in combination with microbubbles is being investigated to promote the local delivery of therapeutic agents as well as to mechanically ablate tissue and enhance thermal therapy. While a diverse range of techniques have been employed, in most circumstances it is the ultrasound-induced dynamic behavior of microbubbles situated within the smallest microvessels that is relevant to achieving the desired therapeutic effects [1–5]. At lower pressure regimes that are typically employed for drug delivery (~<500 kPa), microbubbles generally undergo stable oscillations that produce fluid flow and deformations of the microvascular wall, leading to increases in permeabilization and facilitating the transport of therapeutic agents into the extravascular compartment [6,7]. This is the most widely investigated FUS-mediated microbubble method to date and is the subject of an increasing number of clinical trials [8–10].

As pressure levels are increased, microbubble oscillations become more pronounced and violent inertial cavitation (IC) can occur. Such

* Corresponding authors at: Department of Medical Biophysics, University of Toronto, M5G 1L7, Canada.
E-mail addresses: xxiao.zhao@mail.utoronto.ca (X. Zhao), goertz@sri.utoronto.ca (D.E. Goertz).

https://doi.org/10.1016/j.ultsonch.2023.106291
Received 14 November 2022; Received in revised form 22 December 2022; Accepted 4 January 2023
Available online 5 January 2023

exposures can result in microvascular damage, leading to blood flow shutdown and subsequent tissue necrosis, which has been referred to as nonthermal ablation, antivascular ultrasound, or vascular disruption therapy [11–20]. This emerging approach and the conditions required to initiate it are less understood than drug delivery, but recent evidence supports that vascular disruption is most readily induced in smaller microvessels (<20 μm), with the impact on larger vessels increasing as pressure is elevated [21,22]. This method can potentially be used for a range of applications, with the most investigated to date being in brain tissue [14,15,23] and tumors [20,24–26], where in the latter case it has been shown to enhance the effects of conventional approaches of radiotherapy [27–30], chemotherapy [31–33] and immunotherapy [34,35].

The clinical translation of FUS-mediated microbubble treatments hinges upon the use of cavitation control to ensure efficacy and safety. The underlying premise of cavitation control is that microbubbles exhibit distinct oscillation characteristics leading to certain acoustic emissions that can be detected and used as a basis for modulating ultrasound exposures. This area has been the subject of considerable research in the context of drug delivery [7,36–38]. A prominent control approach is to increase pressure to a level where order 1/2 subharmonic (SH) or 3/2 ultraharmonic (UH) emissions are observed, at which point the transmit amplitude is reduced for successive pulses [39–41]. The rationale for this is the association between the emergence of SHs and UHs with more pronounced oscillations that can induce microvascular damage (e.g. erythrocyte extravasation). Other approaches involve monitoring harmonic signal levels [42], with the assumption that this will correspond to sufficiently pronounced microbubble oscillations to induce permeabilization. This has also been coupled with monitoring for the presence of IC [43,44].

For antivascular therapy, control methods have yet to be established. In a limited number of studies that have monitored emissions in bulk tissue, IC has been shown to be present along with SHs and UHs [23,32,35,45,46]. Several studies have indicated a correlation between IC and either vascular damage or the ensuing tissue necrosis [23,37,47–49]. Interestingly, in recent work using simultaneous multiphoton microscopy and cavitation emission detection, microvascular disruption was also observed to occur in the presence of order 1/3 and 2/3 SHs and 4/3 and 5/3 UHs [50].

To date, the implementation and validation of cavitation control methods have been based on linking emissions and control approaches to bioeffects. It is noteworthy that when this is done the emission signals are derived from the overlapping region of sensitivity of the transmit and receive beams, which is many cubic millimeters in size and can encompass smaller arteries and veins in addition to microvessels. Further, microvessels are typically considered to be vessels of diameters of 100–300 μm and below and include varying calibers of arterioles and venules as well as capillaries. As there is considerable evidence that therapeutic effects are preferentially achieved in the smallest microvessels (<50 μm) [4,21,50,51], it can be argued that the ideal control mechanism should mainly consider the emissions from these microvessels. However, only a portion of the received emissions are from microbubbles in these smaller vessels since they only comprise a fraction of the total blood volume within the region of sensitivity [52,53]. It is therefore of interest to understand the manner in which cavitation varies as a function of vessel diameter under conditions relevant to FUS microbubble-mediated therapies.

It is widely recognized that when microbubbles are situated in microvessels their dynamic behavior in response to ultrasound will differ from when they are in an unconfined state, due to the viscoelastic response of the vessel wall, modifications of fluid microstreaming and inertial coupling to fluid constrained to be within the vessel. This has been examined from a theoretical and modeling perspective in the setting of individual microbubbles at relatively low pressures [54–59]. Ultrahigh-speed (Mframes/s) optical imaging techniques have been an important tool for investigating microbubble behavior in numerous studies, mainly under conditions relevant to imaging or therapy in larger channels (≥200 μm) or chambers [60–66]. There has also been a wealth of ultrahigh-speed optical studies examining microbubble behavior within small vessel phantoms [67–69] and ex vivo capillaries [1,70–73] using short pulse exposures (several cycles). Cavitation emissions from bubble populations have been measured in smaller phantom channels (90–800 μm) in the absence of optical imaging, and it has been shown that IC emission thresholds increase for smaller tubes [74,75]. There are only limited studies with concurrent high-speed optical imaging and cavitation detection of microbubbles in vessel channels [66,76,77], with one directly relevant example being Chen *et al* [76] which investigated the effect of millisecond scale pulses on populations of microbubbles in 200 μm channels. There is however a lack of direct information (optical, emissions) on cavitation in smaller microvessels <=50 μm (the size of vessels most directly affected by therapy) with longer pulses and pressure levels typically used in FUS.

To this end the objective of this paper is to perform an optical and acoustic investigation, using concurrent cavitation detection and high-speed (10 kframes/s) optical imaging, on the behavior of populations of microbubbles situated in small compliant channels (15, 50, 100, 200 and 1200 μm in diameter) under a range of ultrasound exposure conditions that are relevant to antivascular therapy and drug delivery. An emphasis was placed on employing conditions relevant to antivascular ultrasound, as microbubble behavior at higher pressure regimes is poorly understood. Collectively this information is relevant to the interpretation of signals arising from volumes of tissue that contain a range of microvessel calibers - signals that are currently used for cavitation-based control methods.

2. Methods

2.1. Exposure scheme overview

An important aspect of experimental design was the selection of pulsing schemes and pressure ranges. In general, the pulse lengths employed for drug delivery are on the order of 1–10 ms with pressures ranging from 100 to 200 kPa to 400–500 kPa for transmit frequencies in the 0.3–1.5 MHz range [78,79]. However, shorter, more closely spaced pulses have also been employed [80,81]. Antivascular ultrasound pressures and pulsing schemes have varied widely [50] and have included either millisecond scale pulses as well as a series of closely spaced (kHz) shorter pulses (16–100 cycles). In this study, we operate at 1.4 MHz and employ pressures ranging from 0.1 to 3 MPa to cover a range that is relevant to both drug delivery and antivascular therapy. Two pulsing schemes were tested. The first was a single sequential 'short burst' method (100 pulses of 0.102 ms in length spaced at 1 ms) similar to that previously reported in [31,32] for tumor antivascular therapy. The second was a 5 ms pulse, similar to the conditions employed in [50].

2.2. Optical and acoustical setup

An overview of the experimental configuration is shown in Fig. 1(a). High-speed microscopy (Photron Fastcam APX-RS, Olympus LUMPFLN60XW objective, 2 mm working distance) was used to examine the evolving patterns of microbubble behavior under different ultrasound and channel conditions over milliseconds timescales. A framerate of 10 kframes/s was used with a shutter speed of 1 μs to limit the temporal averaging of the high-speed microbubble interactions for clearer images. Brightfield illumination was achieved using a light guide coupled to a xenon flash lamp (Godox QS1200II, 1200 W). The vessel phantom was mounted horizontally on a 3-axis stage within a water tank containing degassed, deionized water. In order to maximize bubble visualization, different optical field of view dimensions were employed depending on channel size: 816x256 μm for the 15 and 50 μm channels, 640x384 μm for the 100 μm channels, and 448x640 μm for the 200 μm channels, with the latter configuration capturing the distal channel wall.

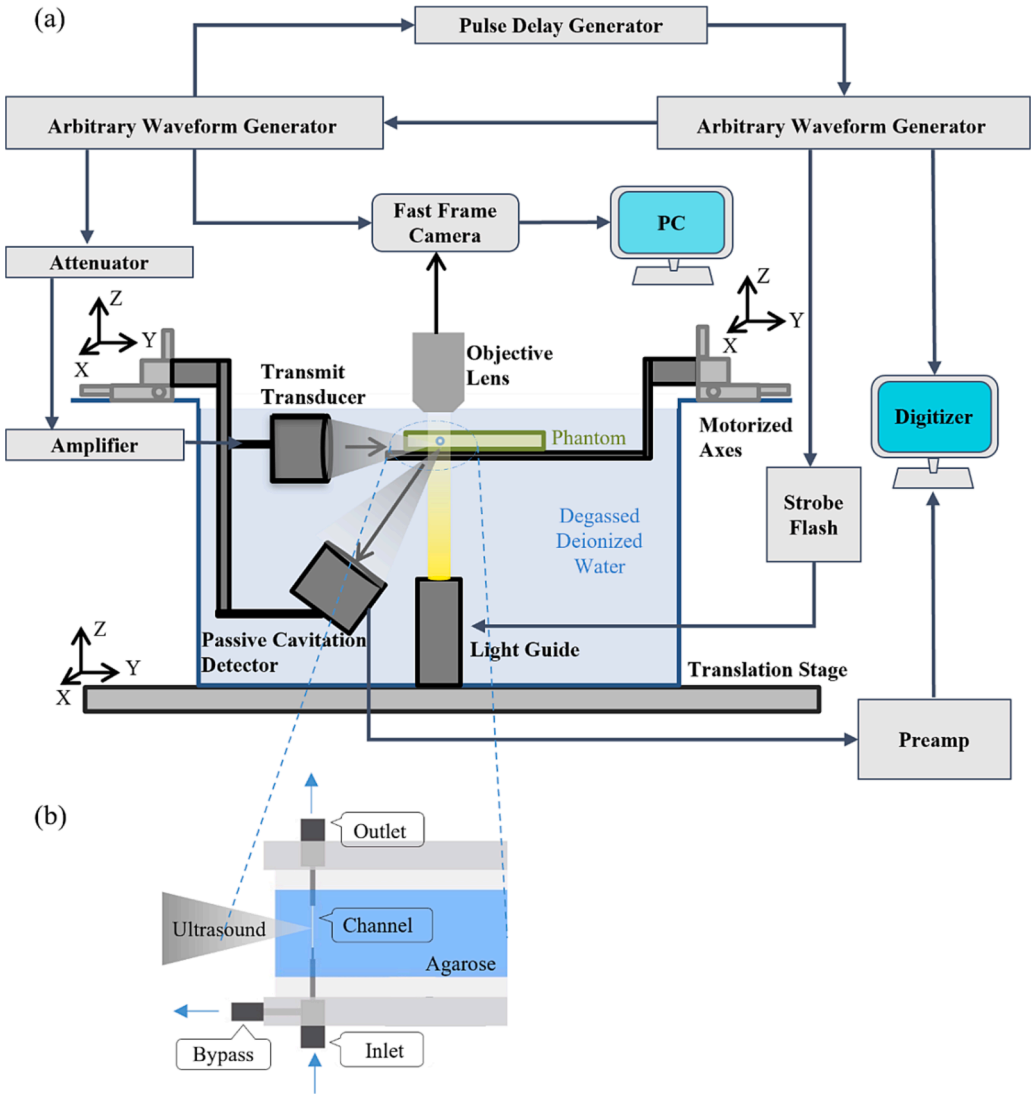

Fig. 1. Schematic diagram of the experimental apparatus showing (a) a side view of the overall experimental setup and (b) a detailed top view of the vessel phantom.

Broadband transmit and receive transducers were configured such that their focal regions overlapped within the optical field of view. The transmit transducer (Olympus C305-SU, 0.75-inch diameter, 1-inch focal length, 2.25 MHz nominal center frequency) was driven by an arbitrary waveform generator (Tektronix AFG3102) and amplified by a 55 dB RF power amplifier (Electronics & Innovation A150, 0.3–35 MHz, 150 W). Peak negative pressures of 0.1, 0.25, 0.5, 1, 1.5, 2, and 3 MPa were calibrated using a PVDF needle hydrophone (Precision Acoustics NH0075). In Supplementary Fig. 1, the relative values of the fundamental, second and third harmonic content as a function of pressure in the focal region are shown. The transducer had a −6 dB beamwidth of 2.5 mm at focus and a depth of field of 13.75 mm as measured with the hydrophone at 1.4 MHz. The −6 dB bandwidth at focus was measured to be 1.25–3.5 MHz.

The acoustic emissions from the bubbles were detected with a broadband receive transducer (Olympus C305-SU; 0.75-inch diameter, 1.5-inch focal length; 2.25 MHz nominal center frequency; −6 dB beamwidth of 3.5 mm at 1.4 MHz). For the 15 and 50 μm channels with transmit pressures up to 1000 kPa, and for 100 and 200 μm channels with transmit pressures up to 500 kPa, received signals were amplified using an 18 dB preamplifier (MITEQ, AU-1433, 0.3–200 MHz) prior to digitization. These acoustic signals were captured using a Picoscope 5000D with a sampling rate of 125 MHz. Signals were recorded for the entirety of the ultrasound pulses, with at least an additional 100 μs from before the arrival of each ultrasound burst to enable an assessment of noise levels. Baseline (control) signals with only saline in the channel were also captured for each experimental condition prior to microbubble injection. The synchronization of illumination, fast-frame imaging, ultrasound transmission, and acoustic emissions recording was accomplished using a second arbitrary waveform generator (Tektronix AFG3022B) and a pulse delay generator (Berkeley Nucleonics Corp. Model 575).

The relationship between the synchronization of the ultrasound and the high-speed camera is shown in Fig. 2 for the two pulsing schemes. For both schemes, the camera frame rate was 10 kframes/s (100 μs/frame), and the shutter time was set to a 1 μs exposure at the end of each frame. Timing of the ultrasound transmission was configured such that 1 frame pre-ultrasound was recorded. For the short pulse scheme, the ultrasound pulse was 102 μs, such that FUS-stimulated bubble behavior was captured during frames 2 and 3 (corresponding to ~0.66–1.66 and ~100.66–101.66 μs of the ultrasound pulse). A 4th frame was captured to visualize the channel post-ultrasound (~99 μs after the end of the pulse). This process was repeated at a 1 kHz interval for a total of 100 bursts. Cavitation signals were recorded for a single sequence of 100 bursts, however, due to limitations of the flash lamp duration, no more than the first 10 bursts were recorded optically for the short pulse

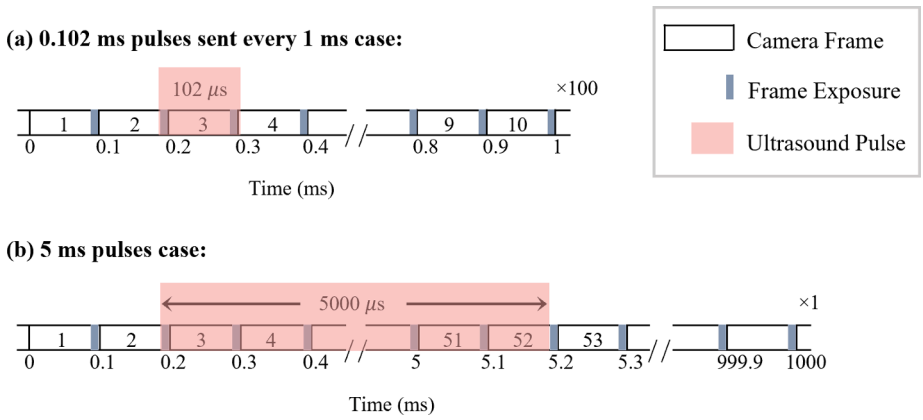

Fig. 2. The timing relationship between high-speed camera frames and arrival of the ultrasound pulse for (a) the 0.102 ms, 1 kHz PRF and (b) 5 ms pulsing schemes. The shorter pulsing scheme shows that the ultrasound sonication is captured in the optical exposure (shaded gray regions) of frames 2 and 3, while the longer pulsing scheme is captured in frames 2 to 51.

scheme. Following the 100th burst, an optical image was captured to enable an assessment of the channel status. For the 5 ms pulsing scheme, bubble behavior was captured optically in frames 2–51 (corresponding to timepoints ~0.66–1.66 to 4900.66–4901.66 μs of the ultrasound pulse). Frames 1 and 52 captured the channel immediately prior to and after the ultrasound pulse respectively. One burst of 5 ms pulses was recorded both optically and acoustically.

2.3. Small vessel phantom

The vessel phantom (Fig. 1(b)) employed was a wall-less channel cast within 2.5 % agarose gel. The gel was bounded and held in place with an optically and acoustically transparent polyester film (Mylar, 0.5 mm thickness), which was mounted within an acrylic frame that enabled positioning and attachment of the inflow and outflow ports. The channels were cast with a tungsten wire (with a diameter of the described channel) situated within and between two hollow telescoping tubes made of extracted 23–32 gauge hypodermic needles, depending on desired channel size. After the gel had set, the wire was extracted leaving inflow and outflow ports through the smaller channel over a distance of 4–8 mm. A bypass port was added at the proximal side of the vessel inlet to redirect the flow to a large diameter outlet port. This allowed the inlet tubing to be flushed with the fresh agent before each experiment and saline after each experiment, without having to pass the entirety of the flushing liquid volume through the micron-scale vessel.

2.4. Microbubble preparation and handling

Experiments were performed using the widely employed commercial contrast agent Definity® (Lantheus Medical Imaging), a polydisperse suspension of phospholipid-encapsulated octafluoropropane microbubbles. The vials were activated through mechanical agitation for 45 s using a VialMix® (Lantheus Medical Imaging) activation device. For experiments using the native Definity sample, the vial was inverted for 30 s and a 100 μL volume was extracted each time and diluted by a factor of 5000 in saline according to previously described methods [82].

In addition, the short pulse scheme experiments were repeated with a 'nanobubble' subpopulation of native Definity, which was isolated using an Acrodisc® syringe filter (Pall Laboratory, supor membrane, 0.45 μm pore size). In this case, the vial was inverted for 2 min before extracting a 200 μL volume which was then diluted 10 times prior to passing through the filter, similar to a procedure reported in [83]. The dilution ratio was chosen to approximately volume-match the nanobubbles to the diluted native Definity microbubble solution.

Coulter Counter size measurement data for native and filtered Definity populations are shown in Supplementary Table 1 and Supplementary Fig. 2. In both cases, diluted agent was gently introduced into the channel via a syringe through the inflow port with an open outflow port. The outflow port was then closed while measurements were performed. Between measurements, the outflow port was opened, agent was replenished within the channel, and the outflow port was closed again.

2.5. Data processing

2.5.1. High-speed microscopy

The temporally uneven illumination intensity of the flash lamp was corrected by adjusting the contrast and brightness of each frame using a MATLAB (The MathWorks Inc., MA, USA) script.

2.5.2. Cavitation signals

The received cavitation signals were processed in MATLAB. All signals were first filtered with a 5th-order 0.3–10 MHz Butterworth bandpass filter. For the short burst scheme, the emission spectra were derived from a Fast Fourier Transform (FFT) of a 102 μs Hanning window segment that was zero-padded to the next power of 2 from its original length, resulting in a frequency resolution of 7630 Hz. For the long burst scheme, a 5 ms segment corresponding to the cavitation signals underwent an FFT resulting in a frequency resolution of 200 Hz. This process was done both for baseline (saline only) and for bubbles. Noise and baseline signals were subtracted from the bubble cavitation data for presentation and quantification purposes.

To analyze the temporal evolution of the bubble cavitation within pulses, sliding Hanning windows of 20 μs for the short burst scheme and 100 μs for the 5 ms pulses were applied every 10 μs and 50 μs, respectively (corresponding to 50 % overlap). Each window was zero-padded to the next power of 2 from its original length before undergoing an FFT, resulting in frequency resolutions of 30518 Hz and 7629 Hz, respectively.

Cavitation within selected frequency bands was quantified by computing the mean power over 50 kHz windows centered at the order 1/2 SH (0.7 MHz), fundamental (1.4 MHz), order 3/2 UH (2.1 MHz), and second harmonic (2.8 MHz) frequencies, as well as a frequency range away from these peaks at 1.925 to 1.95 MHz and 3.01 to 3.035 MHz as an indicator of IC. The ratio of the SH mean to the mean of its surrounding IC (0.575 to 0.6 MHz and 0.8 to 0.825 MHz) was used as an indicator of 'relative' SHs, and the ratio of the UH mean to the mean of its surrounding IC (1.975 to 2 MHz and 2.2 to 2.225 MHz) was used as an indicator of 'relative' UHs. Each mean was normalized to its corresponding lowest pressure mean. To quantify the cavitation levels for each channel diameter as a function of time within pulses or as a function of burst number, the cavitation was normalized with respect to the

baseline value.

Spectrograms were used to illustrate the evolution of bubble activity over time. For the short pulsing scheme, the entirety of each pulse was used as the window. For the 5 ms pulses scheme, 100 μs windows every 50 μs were applied across the 5 ms pulse. The frequency domain noise and baseline signals were subtracted from the bubble spectra which were then normalized at each pressure to the maximum signal across all channel sizes.

3. Results

A summary of the experiments conducted is shown in Supplementary Tables 2–4. An emphasis was placed on acquiring data for the short pulse sequence for both agent types and all channel sizes. These data were supplemented with 5 ms experiments for a subset of conditions.

3.1. Short pulse sequence (native Definity)

The results in this section look at the response of native Definity to the short pulsing scheme with changing pressures and channel sizes. We begin by examining spectral and optical features of the data for earlier pulses in the sequence before describing the evolution over the sequence.

3.1.1. Spectral and optical data

Fig. 3 shows the averaged cavitation spectra of the first five bursts for different acoustic pressures and channel diameters. In these spectra, there are clear peaks at the fundamental, second and third harmonics, which increase in magnitude with pressure. The harmonics will be due to a combination of emissions from the bubbles, along with scattering from propagation harmonics (Supplementary Fig. 1) that are incident on the bubbles. Generally, for each channel diameter there is a pressure threshold at which there is a distinct jump in the magnitude of broadband noise signals (IC). This pressure threshold tends to increase with decreasing channel diameter. For example, for a 15 μm channel diameter a minimum pressure of 1.5 MPa is required before a significant rise (>20 dB) in broadband signal relative to baseline is observed, whereas for a 1200 μm channel, a rise in IC is seen at only 250 kPa. For 50 and 100 μm channels, the IC rises at 1 MPa, and for 200 μm a rise is seen at 500 kPa.

There are also trends in the development of SHs and UHs as a function of pressure and channel diameter. Similar to IC, the emergence of SH and UH signals tend to increase with pressure with a similar pressure threshold of IC for smaller diameter channels. For example, in 15 μm channels, distinct 1/2 order SHs and 3/2 UHs are seen only at 1.5 MPa and above; in addition to 1/2 order SHs and 3/2 UHs, their third order 2/3 SHs and 4/3 and 5/3 UHs are visible at 3 MPa; 11/9, 9/7, 12/7, and 16/9 UHs are visible at 2 MPa; 6/5, 9/7, 12/7, and 9/5 UHs are seen at 1.5 MPa. A number of SHs and UHs are also faintly visible in 50 μm channels at 2 and 3 MPa, and even more faintly in 100 and 200 μm channels (features are summarized in Supplementary Table 2). The 1200 μm channels show a distinctly different pattern, with 3/2 UHs arising at 100 kPa and 1/2 SHs becoming visible beginning at 250 kPa. The SHs and UHs are however no longer visible at higher pressures of 1 and 1.5 MPa in the 1200 μm channel.

Fig. 4 shows a quantification of the magnitudes of relative 1/2 SHs, relative 3/2 UHs, and IC power bins evolving as a function of pressure and channel diameter. The pressure threshold for the elevation in IC decreases as the channel diameter increases. The IC level continues to increase with pressure before leveling off at ~ 1.5 MPa. The relative SHs and UHs show similar behavior to the IC power trend in 15 μm channels, but appear to reach a peak at 2 MPa. The relative SH and UH levels are present for the 50 μm channel at higher pressures (>1 MPa) but substantially reduced compared to the 15 μm case. For the 100 and 200 μm channel sizes, pronounced SHs are not present, though modest levels of UHs do appear at higher pressures. For the 1200 μm channel, the power levels of relative SHs and UHs increase to a maximum at 250 kPa before decreasing as the pressure level increases further. We note that, due to the presence of incident propagation harmonics complicating the interpretation of harmonic bubble emissions in these bandwidths, the harmonic regions have not been quantified.

Fig. 5 shows representative successive microscopy frames for

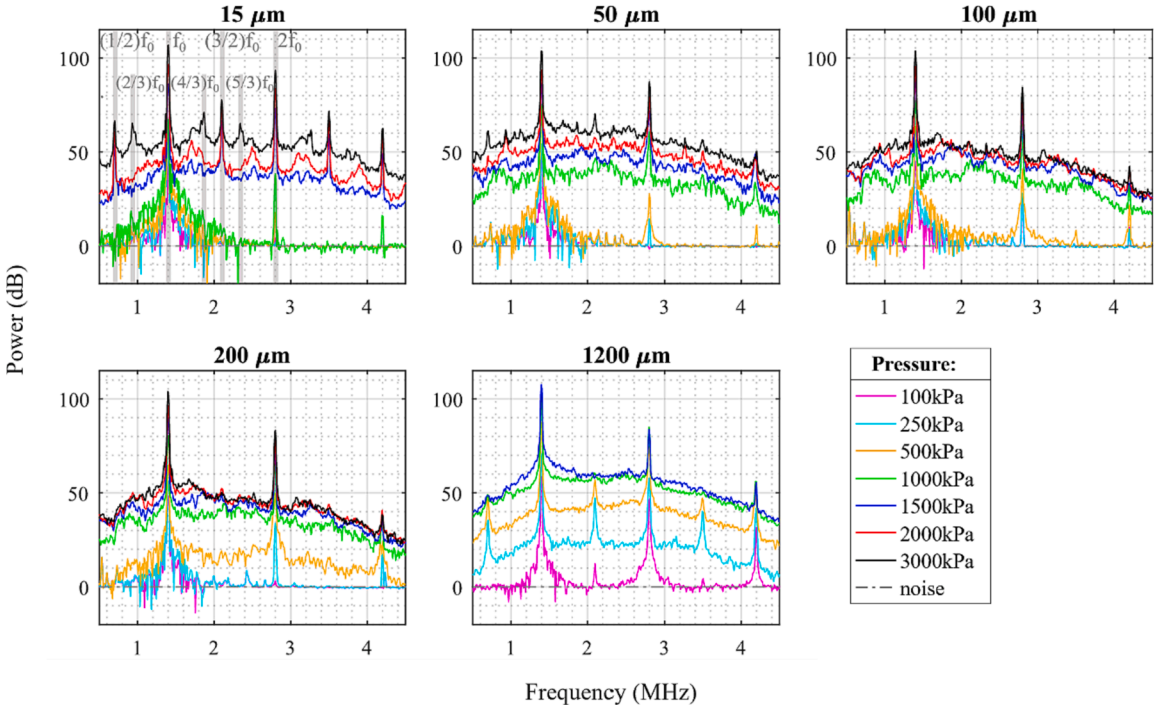

Fig. 3. Cavitation spectra for the average of the first five bursts of the 0.102 ms pulsing scheme of native Definity for different sonication pressures and channel diameters. Gray-shaded regions in the 15 μm channel pane highlight different frequency peaks with fundamental frequency f_0.

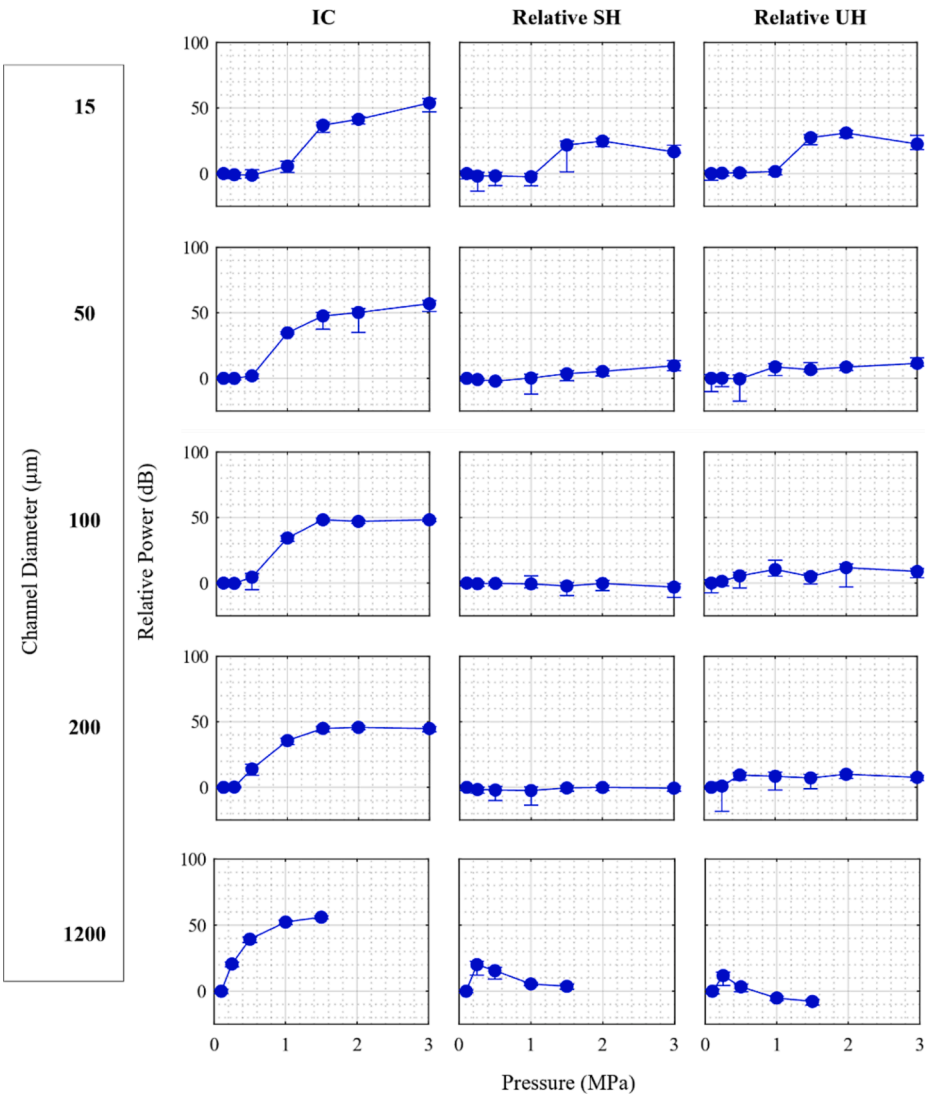

Fig. 4. Mean of power from first 5 bursts for selected frequency bands for native Definity as a function of sonication pressure for different channel diameters for the 0.102 ms pulsing scheme, normalized within each pane to the corresponding power at 100 kPa. Error bars represent standard deviation.

different channel diameters and pressures for the first pulse. As bubbles prior to sonication are smaller and distributed at different depths within the channel, they are typically not visible within the optical focal plane. For each channel diameter, visible bubble expansion during sonication only occurs past a certain pressure threshold, which increases as the diameter decreases. For example, with the 15 μm channel, no bubble expansion is visible during sonication until 1 MPa, with larger expansion visible at 1.5 and 2 MPa and yet more activity at 3 MPa. In the 200 μm channel, expansion is seen at 500 kPa, with bubble activity increasing significantly with pressure. The intermediate channel diameters show clear bubble activity starting at 1 MPa and similarly increased activity with pressure beyond this threshold. At pressures where bubble activity is optically evident, it manifests as discrete centers of expanded bubbles in the first image frame (consistent with spatially separated individual bubbles), followed by the emergence of what can be described as clusters or clouds of bubbles at later frames (subsequently referred to as clusters).

In the case of the larger channels (100 and 200 μm) there was a translation of bubbles and the corresponding accumulation of bubbles and clusters at the distal wall. In the smaller channels (15 and 50 μm), the clusters occupy the entire channel diameter, appearing to induce deformation on the channel walls (both sides in Supplementary videos 1–2, right side in Supplementary videos 3–4). A quantification of the cluster dimensions for the 15–100 μm channels at 2 and 3 MPa is shown in Supplementary Table 5. Post-sonication, what appear to be residual bubbles are present in the previous location of the clusters (visible in Supplementary videos 1–3 post sonication). It should also be noted that non-spherical bubble expansion could be observed (Supplementary videos 2–3).

The pressure thresholds for the optically observable bubble expansion are slightly lower than the thresholds for the onset of broadband emissions seen in the spectral data of Fig. 3. The behavior of the bubbles in Fig. 5 also appears different throughout sonication. To better understand these findings, Fig. 6 shows the temporal evolution of cavitation spectra for the average of the first five bursts. A notable feature is that for the pressures at which a rise in the IC is first seen (1 MPa for 15 μm and 500 kPa for 200 μm), the magnitude of the broadband signal decreases after the first 20 μs. In 15 μm channels at 3 MPa, 2/3 SHs and 4/3 and 5/3 UHs increase in magnitude at later sonication times. In the 200 μm channel, at 250 kPa, distinct 3/2 UHs appear in the 0–20 μs spectra but not at later sonication times. The pressure threshold at which a rise in IC is seen in the 0–20 μs spectra matches with the optically observed pressure threshold for bubble expansion.

3.1.2. *Evolution of data over the full pulse sequence*

Fig. 7 shows spectrograms as a function of burst number for different

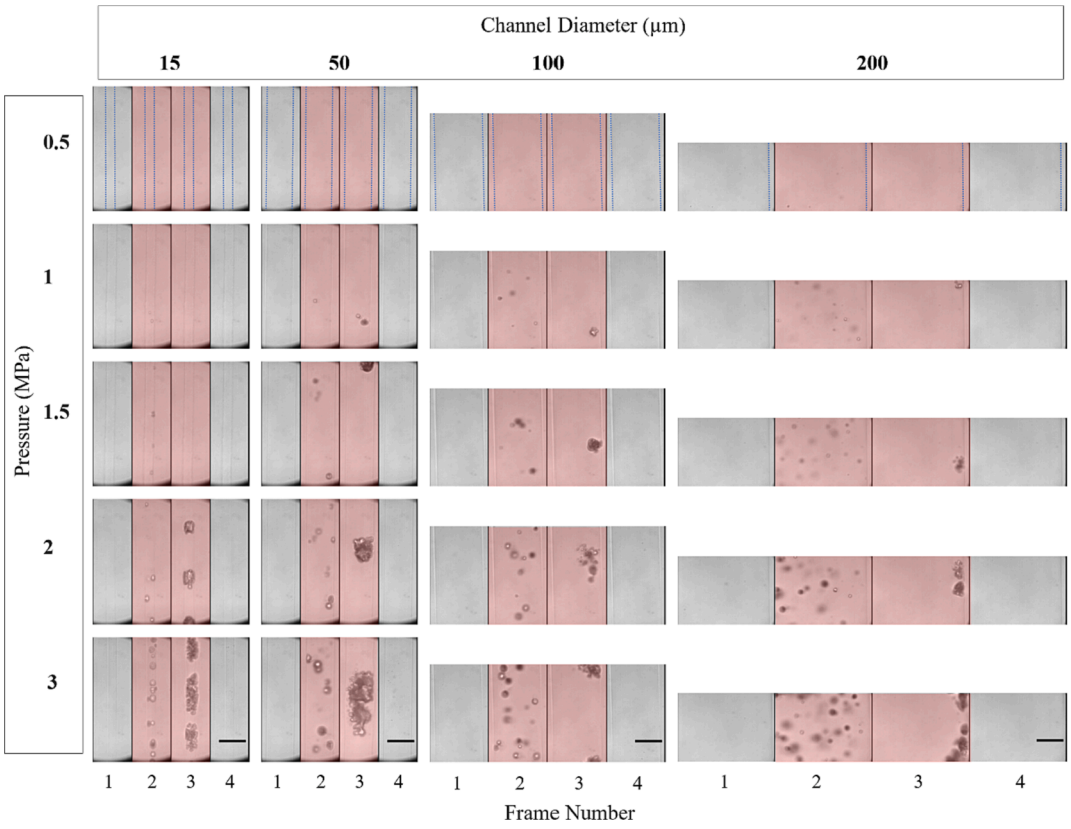

Fig. 5. Representative optical images from high-speed microscopy showing native Definity bubble activity during the first burst of the 0.102 ms pulsing scheme for different sonication pressures and channel diameters. Frames are separated by vertical black lines and red shaded frames indicate ultrasound exposure. Dashed blue lines in the first row indicate the boundary of the channel diameter. Scale bars on the bottom row represent 50 μm. (For interpretation of the references to colour in this figure legend, the reader is referred to the web version of this article.)

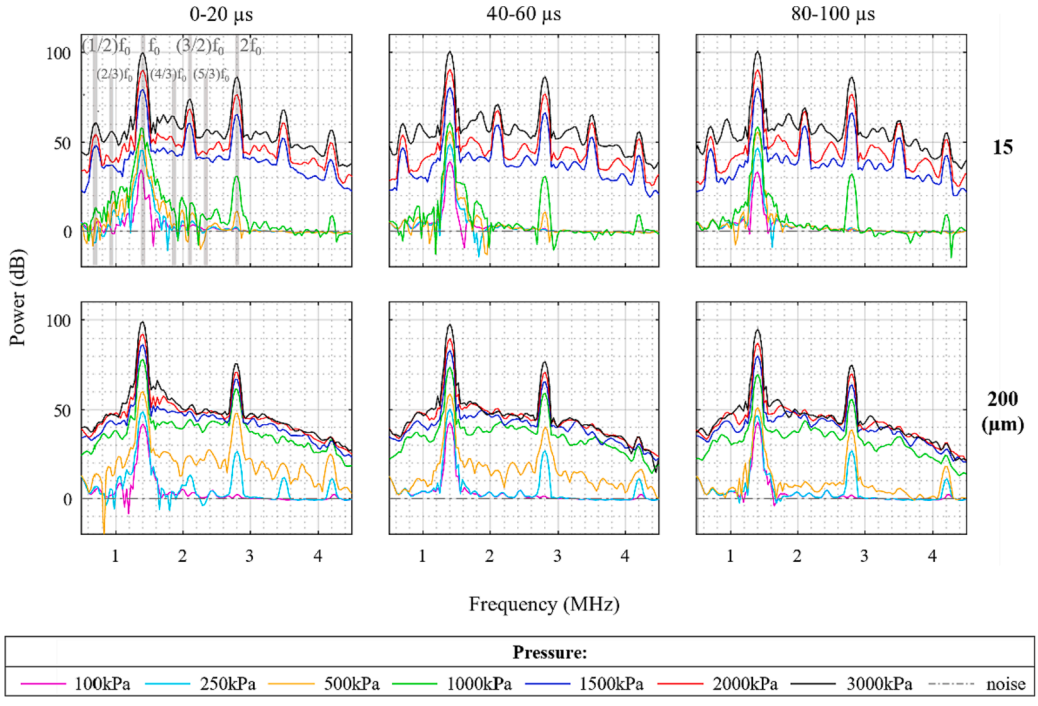

Fig. 6. The temporal evolution of the native Definity cavitation spectra within pulses for the 0.102 ms pulsing scheme for different sonication pressures and channel diameters. Gray-shaded lines in the 15 μm channel pane indicate different frequency peaks with fundamental frequency f_0. Derived from the average of the first five bursts.

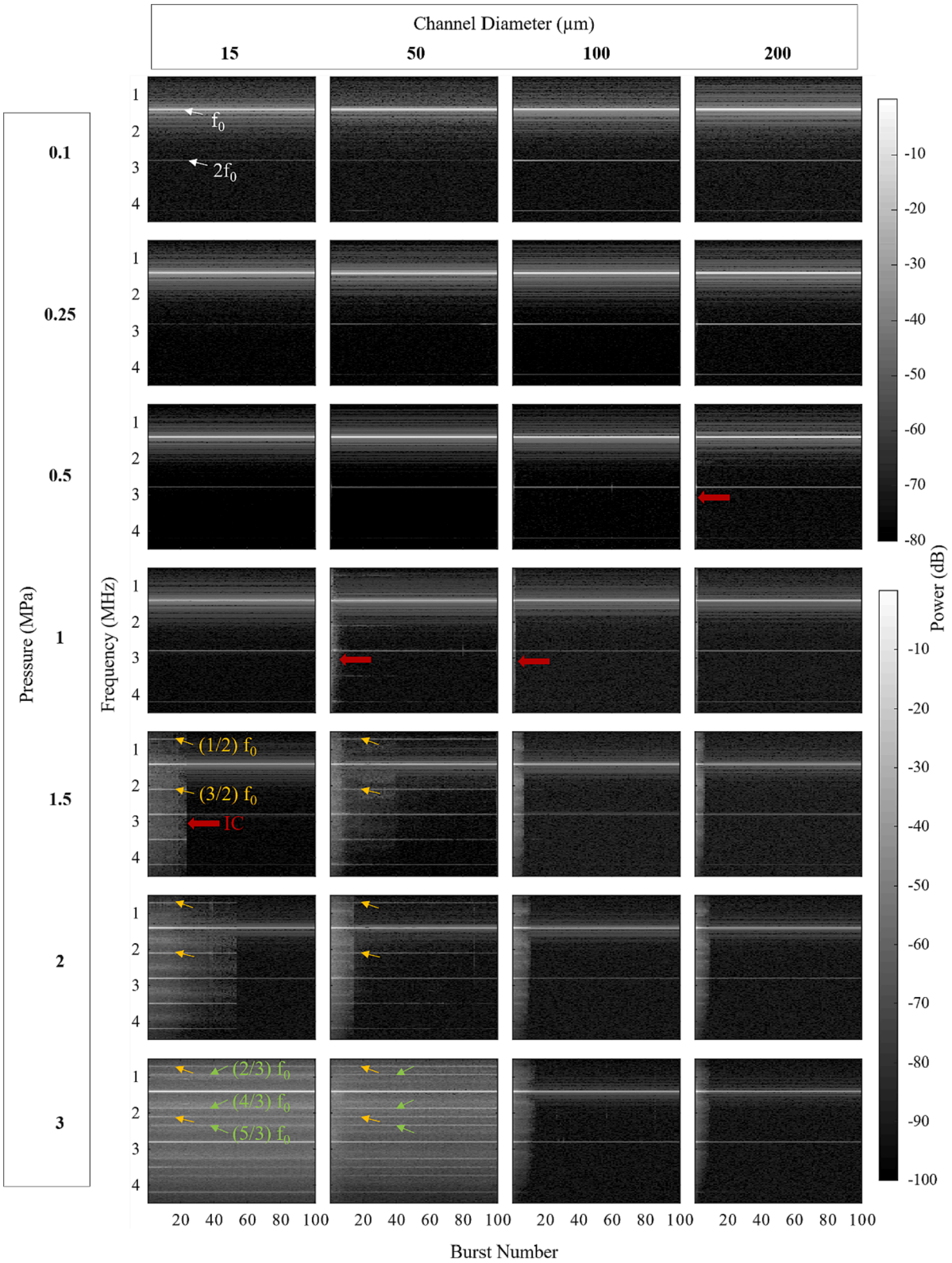

Fig. 7. Spectrograms of the native Definity cavitation signals for the 0.102 ms pulsing scheme over sequential bursts for different sonication pressures and channel diameters. White arrows point out fundamental f_0 and second harmonics $2f_0$. Yellow arrows point out second-order SHs and UHs, green arrows point out third-order SHs and UHs, and red arrows highlight areas with inertial cavitation. Results are averaged over all acquisitions for each condition. (For interpretation of the references to colour in this figure legend, the reader is referred to the web version of this article.)

pressures and channel diameters (≤200 μm). This data is supplemented by an analysis of the persistence of specific frequency bands in Supplementary Fig. 3. The results for the earlier pulses (≤5) exhibit increased spectral content (IC, SHs, UHs) at higher pressure levels, consistent with Fig. 3. For the 100 and 200 μm channels the broadband spectral features that are present for pressures ≥ 500 kPa in early pulses decrease to noise levels within 20 pulses (depending on pressure). A similar pattern is also observed for the 1200 μm channel as can be seen in Supplementary Fig. 4. These results contrast with the 15 and 50 μm channel data which show that once IC, SHs, and UHs have developed (1–1.5 MPa) there is an increased persistence with pressure. At 3 MPa the IC, SHs, and UHs persist over the entire 100-burst sequence.

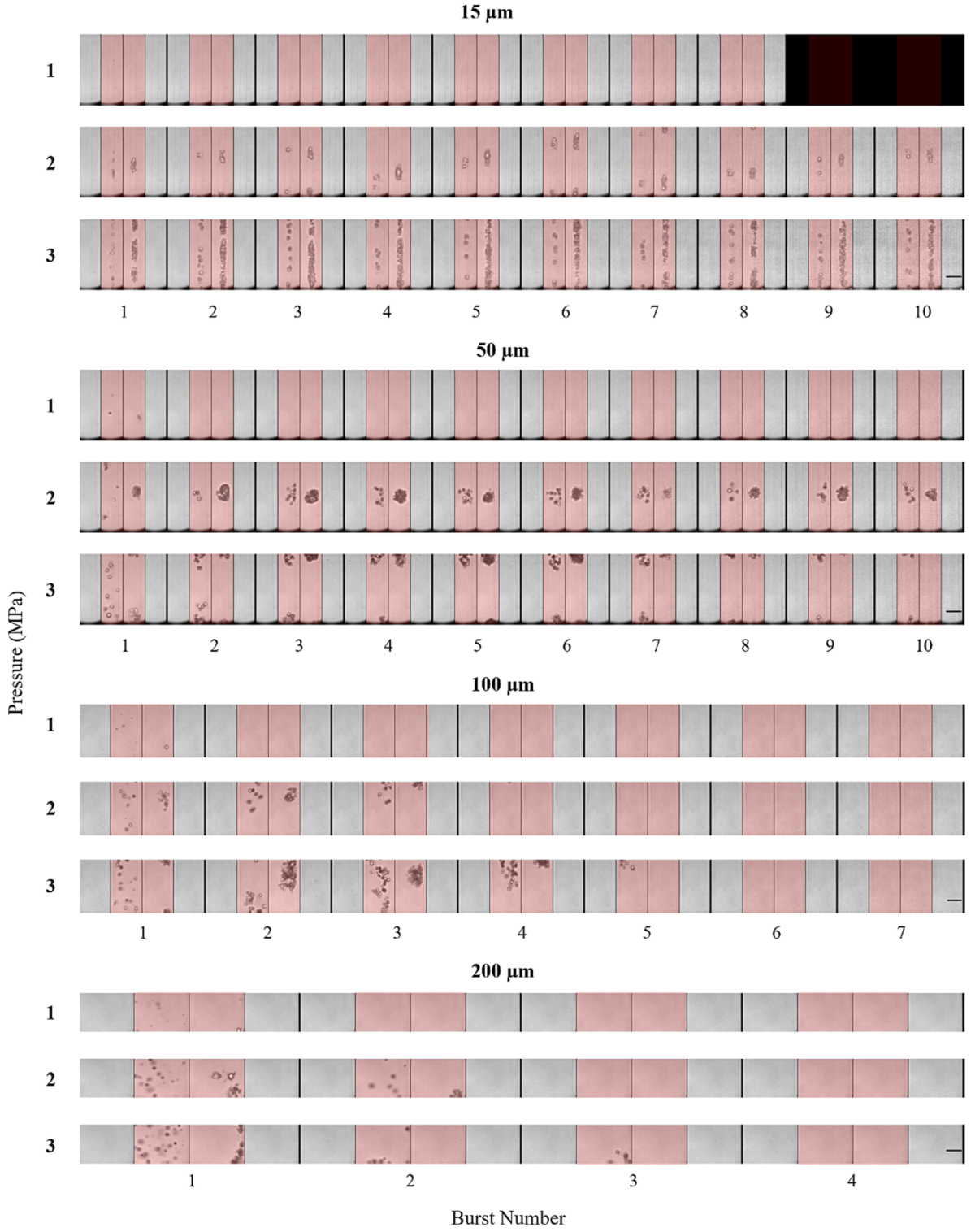

Fig. 8. Representative optical images from high-speed microscopy showing the evolution of native Definity bubble activity over sequential bursts of the 0.102 ms pulsing scheme for different sonication pressures and channel diameters. The 4 frames within each burst are separated by thin vertical black lines, while thicker vertical black lines separate bursts. Frames shaded red denotes the presence of ultrasound sonication. Scale bars on the bottom rows represent 50 μm. (For interpretation of the references to colour in this figure legend, the reader is referred to the web version of this article.)

Fig. 8 shows concatenated optical images for successive bursts. These images show the pressure and channel size dependence on bubble behavior, and the complex bubble patterns produced over multiple bursts. Similar to Fig. 5, the bubbles are not visible until the first frame of sonication of each burst where the bubbles undergo expansion, and in the next frame the expanded bubbles translate and cluster in elongated patterns oriented along the channel axis. In the frame immediately post sonication residual bubbles are visible. This pattern repeats over subsequent bursts with new clusters forming in the location of the previous residue, and depending on pressure and channel diameter, the bubbles eventually dissipate at later bursts. The repetition of this cycle of formation and dissipation of clusters persists across all 10 bursts acquired in the 15 and 50 μm channels for the 2 and 3 MPa exposures, but does not at lower pressures and for larger channels. This pattern is consistent with the persistence of IC, SH, and UH emissions shown in Fig. 7 and Supplementary Fig. 3. Representative sonication videos for each channel size at 3 MPa can be seen in Supplementary videos 1–4. A notable observation was that the boundaries of the channels would deform over the course of insonation (Supplementary video 1). Permanent expansions of the 15 μm channel were also observed at 3 MPa (Supplementary Fig. 5), which is consistent with a form of damage induced by the bubbles. No damage was evident at lower pressures for the 15 μm channel or at any pressures for the larger channels.

3.2. Short pulse sequence (filtered Definity)

3.2.1. Spectral and optical data

Fig. 9 shows the cavitation spectra for filtered Definity as a function of channel sizes and pressures, which is quantified for the IC, relative 1/2 SHs and 3/2 UHs in Supplementary Fig. 6. Similar to native Definity, there is a channel diameter-dependent pressure threshold for IC, however this threshold is higher than that of native Definity under the same conditions. This pressure threshold is 2 MPa for 15 μm, 1.5 MPa for 50 μm, 1 MPa for 100 and 200 μm, and 500 kPa for 1200 μm. Similar to native Definity, SH and UH emissions are not evident in the 100 and 200 μm channels but are present in the smaller channels, although they have higher onset pressures (2 MPa). In the 15 μm channel at 3 MPa there are clear peaks at the 1/2, 2/3 SHs and 3/2, 4/3, 5/3 UHs, while at 2 MPa these peaks shift away and appear to be at the 1/2, 3/4 SHs and 3/2, 5/4, 7/4 UHs. A number of distinct SHs and UHs also appear in the 50 μm channels starting at 2 and 3 MPa respectively (Supplementary Table 3). Less prominent SHs and UHs are seen in the 100 μm channel above 1.5 MPa, while no clear SHs or UHs are visible at any pressures in the 200 μm channel. The 1200 μm channel shows 1/2 SHs and 3/2 UHs only at 250 kPa.

Fig. 10 shows successive frames from high-speed microscopy of the sonication at different channel diameters and pressures. As for native Definity, filtered bubbles are not observed until a pressure threshold is reached, which decreases with increasing channel diameter. These optical pressure thresholds are consistent with the spectral IC thresholds seen in Fig. 9. There is a similar pattern of expanded bubbles being present at discrete locations but with a greater density than native Definity. This is followed in the second frame by clustering and - in the cases of 100 and 200 μm channels - an accrual at the distal portion of the channels.

3.2.2. Evolution of data over the full pulse sequence

Fig. 11 shows the spectrograms as a function of burst number at different pressures and channel diameters (≤ 200 μm). Similar to native Definity, spectral activity increases with pressure, and IC tends to persist for a greater number of bursts in smaller diameter channels. In the filtered Definity case, SHs and UHs appear only when IC is also present. 2/3 SHs, 4/3 and 5/3 UHs also appear at 3 MPa in 50 μm channels in the middle of sonication time, but are less prominent compared to native Definity. As a comparison, Supplementary Fig. 7 shows a spectrogram of the 1200 μm channel, where 1/2 SHs and 3/2 UHs only persist around 10 bursts at 250 kPa, IC starts to appear at 500 kPa and persists <10 bursts for pressures 500–2000 kPa. Supplementary Fig. 8 shows the evolution of power for specific frequency bands as a function of burst number which broadly parallels the patterns observed for native

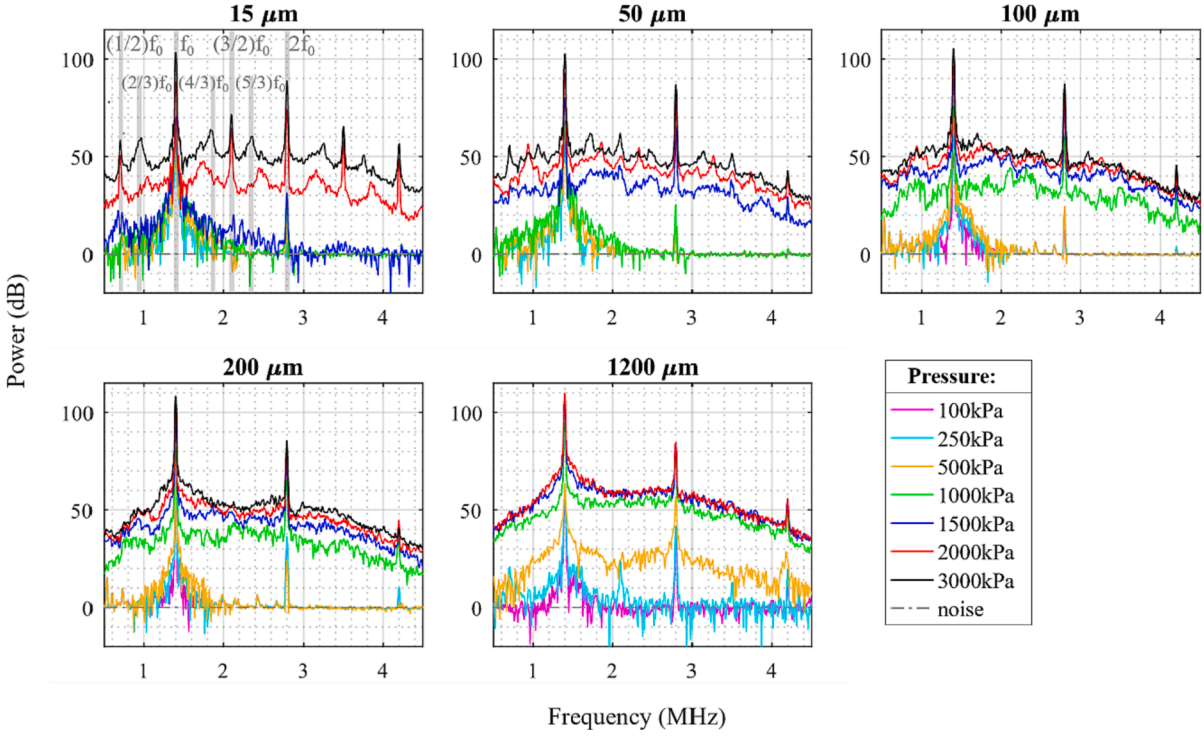

Fig. 9. Cavitation spectra of filtered Definity for the average of the first five bursts of the 0.102 ms pulsing scheme at different sonication pressures and channel diameters. Gray-shaded lines in the 15 μm channel panel indicate different frequency peaks with fundamental frequency f_0.

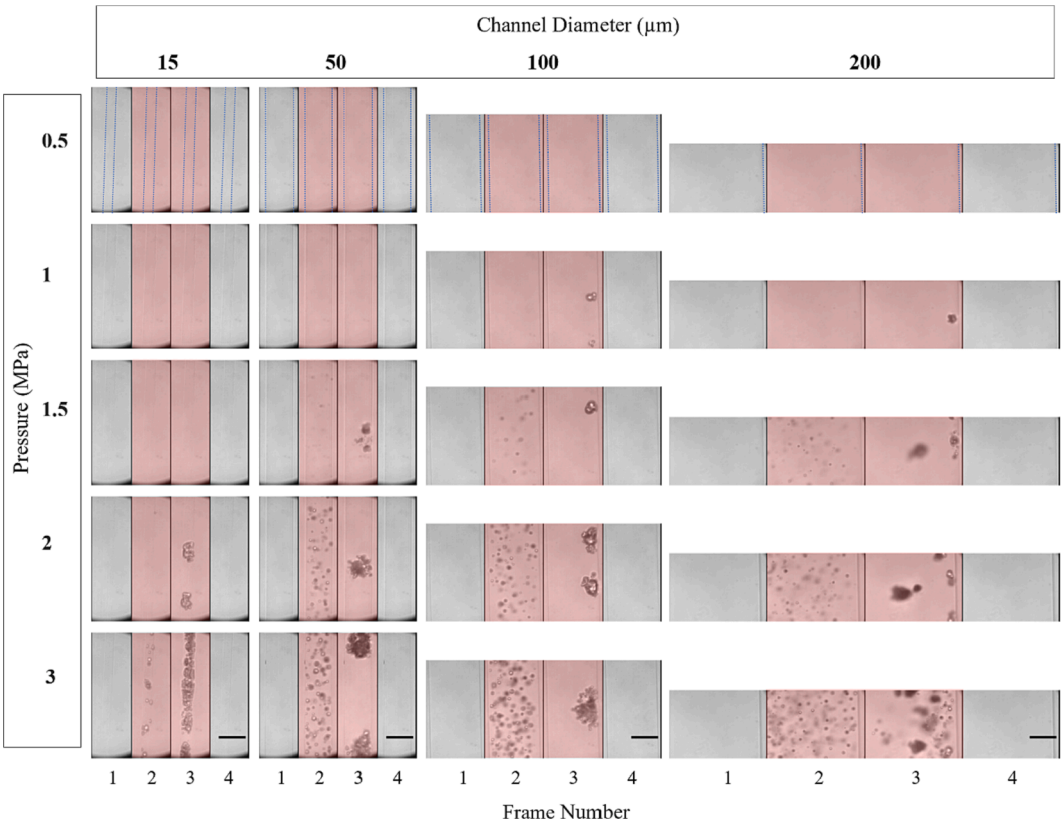

Fig. 10. Representative optical images from high-speed microscopy showing filtered Definity bubble activity during the first burst of the 0.102 ms pulsing scheme for different sonication pressures and channel diameters. Individual frames are delineated by vertical black lines and red shaded frames indicate frames acquired during ultrasound exposure. Dashed blue lines in the first row indicate the boundary of the channel diameter. Scale bars on the bottom row represent 50 μm. (For interpretation of the references to colour in this figure legend, the reader is referred to the web version of this article.)

Definity. Supplementary Fig. 9 shows concatenated optical images from successive bursts, which has a similar pattern as native Definity. Supplementary videos 5 and 6 show representative sonications of filtered Definity in 15 and 200 μm channels at 3 MPa. Unlike the case for native Definity, the 3 MPa pressure level did not result in obvious wall damage.

3.3. 5 millisecond pulse results (native Definity)

Fig. 12 shows spectrograms for the 5 ms pulsing scheme at different pressures for the 15 and 200 μm channels. In the 15 μm channel, IC does not appear until 1.5 MPa, and at that pressure it persists for the entire duration of the pulse. For the 200 μm channel, IC is initiated at 500 kPa and becomes more prominent at 1 MPa and 1.5 MPa. Notably, it persists for <2 ms at these pressures. Order 3/2 UHs are observed and persist for the full pulse length at 500 kPa and 1 MPa, even after the IC has subsided. 1/2 SHs, 3/2, 5/4, and 7/4 UHs are visible in the 15 μm channel at 1.5 MPa (see summary in Supplementary Table 4). Supplementary Fig. 10 shows the cavitation spectra for the first burst at sonication pressures below 2 MPa. For the 200 μm channel, distinct 3/2 UHs appeared at 500 kPa, which were not evident for the short pulse sequence (Fig. 3). However, an examination of the cavitation spectra for the first 100 μs window of the 5 ms pulse (Supplementary Fig. 11) shows the spectra characteristics are very similar to those in Fig. 3 except for the amplitude difference in IC power. Supplementary Fig. 12 shows how the magnitudes of IC power, relative 1/2 SHs, and 3/2 UHs evolve as a function of pressure. Supplementary Fig. 13 shows these relative power bins evolving as a function of time over the first burst of the 5 ms pulsing scheme with different sonication pressures, indicating that the 3/2 UH appears after 0.1 ms and persists for the rest of the 5 ms pulse at 500 kPa.

Fig. 13 shows frames from high-speed microscopy of the longer pulse sonication for 15 and 200 μm channels at 0.5, 1, and 1.5 MPa. In the 15 μm channel, bubble expansion was not observed until 1.5 MPa, where bubbles are seen in the first frame of ultrasound exposure followed by the formation of larger clusters in the next frame which then persist for the duration of the pulse. This persistence of IC throughout the pulse is consistent with the spectrogram data in Fig. 12. The clusters formed in the 15 μm channel are centered within the channel and are of a size greater than the initial channel diameter, resulting in wall displacements during the pulse (Supplementary video 7). In the 200 μm channel, bigger bubbles (1–5 μm) were visible in their quiescent state pre-sonication, then at pressures below the bubble expansion threshold these visible bubbles were observed to continually translate in the direction of ultrasound propagation during sonication (Supplementary video 8). Further, continually oscillating bubbles were observed during the whole 5 ms sonication at 0.5 MPa (Supplementary video 9), corresponding to the persistence of SHs and UHs along the whole pulse. Expanded bubbles are observed in the first frame of ultrasound exposure for 1 and 1.5 MPa, and by the second frame they have translated and clustered at the distal wall (Supplementary video 10). Clusters were no longer observed within the field of view after a few frames, shorter than the duration of measured IC emissions.

At 1.5 MPa, channel damage occurred in the 15 μm channel in the form of sustained circumferentially symmetric localized channel dilations (20–25 μm diameter) at the locations where cluster activity was present (Supplementary Fig. 14). Data above 1.5 MPa (e.g. at 2 and 3 MPa) were not systematically acquired as this would have required channels to be fabricated for each data point due to the presence of damage. Wall damage was not observed in the 200 μm channel.

4. Discussion

Collectively the data have shown that bubble emissions and optically

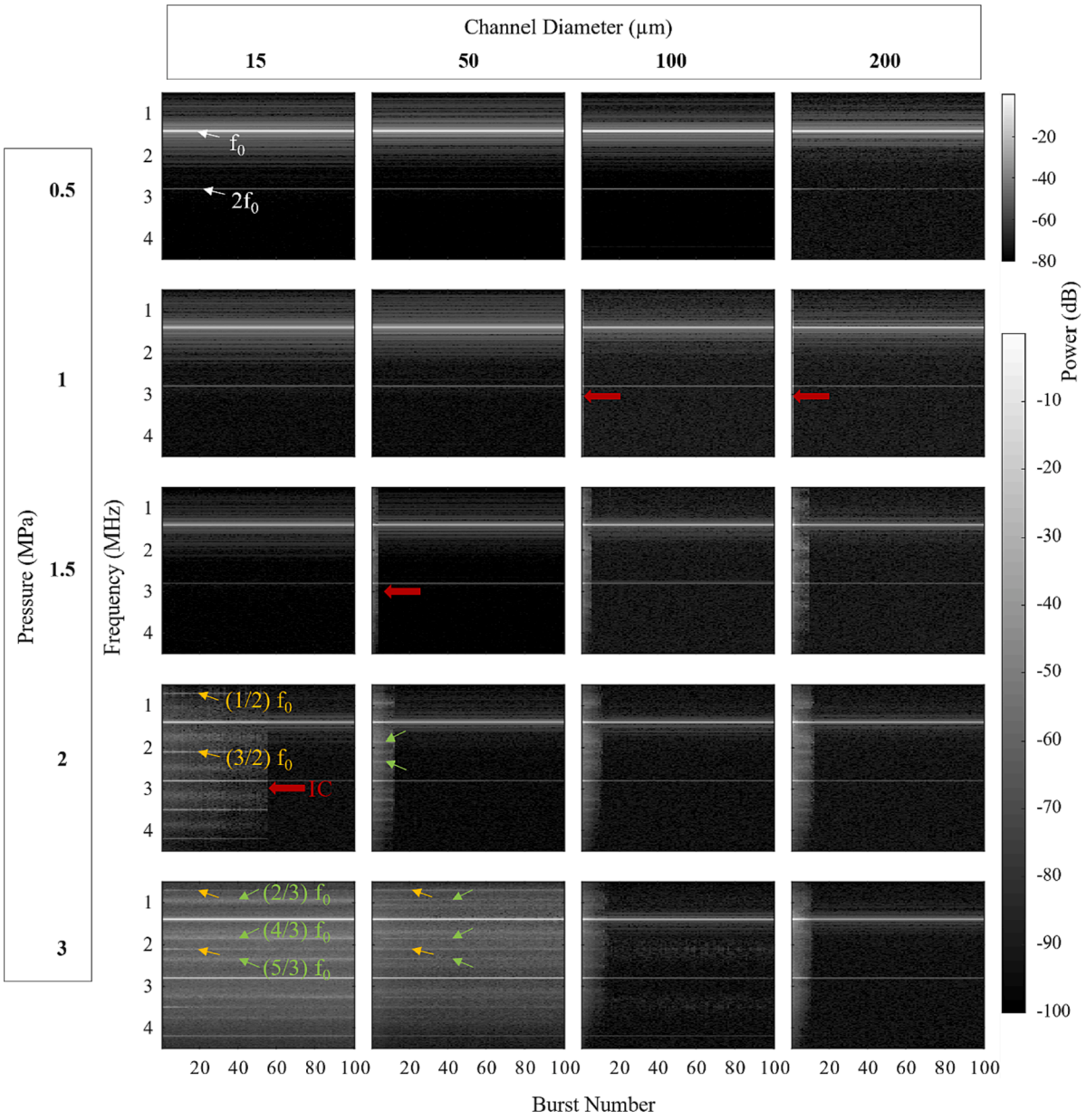

Fig. 11. Spectrograms of the cavitation signals from filtered Definity with the 0.102 ms pulsing scheme for different sonication pressures and channel diameters. White arrows point out fundamental f_0 and second harmonics $2f_0$. Yellow arrows indicate second-order SHs and UHs, and green arrows indicate third order SHs and UHs and red arrows highlight areas with IC. (For interpretation of the references to colour in this figure legend, the reader is referred to the web version of this article.)

observed behaviors are strongly dependent on channel size, with the first transition evident between the dimensions of small arteries (1200 μm) and larger microvessels (200 and 100 μm) and another when diameters were decreased to 50 and 15 μm - on the order of vessel sizes that are impacted by therapy. These data are relevant to improving an understanding of microbubble behavior in the context of FUS treatments that impact the microvasculature. This is particularly the case for the poorly understood antivascular higher pressure regimes (>1 MPa), where both the emission signal strength and improved bubble visualization enable more robust insights than for the lowest pressures. As the channel sizes span the vessel ranges that can be present within the regions used to derive cavitation signals for FUS, they also provide information relevant to the interpretation of emissions that are used for monitoring and control of therapy.

It is useful to first consider the influence of channel size on spectral emissions from native Definity, in particular SHs, UHs, and IC. The 1200 μm channel is the size of a small artery or vein and is also in a range that is commonly used to assess agent behavior or to provide information relevant to implementing cavitation controllers [38]. With this channel for the short pulse sequence (0.1 ms), there was an onset of detected 1/2 SH, 3/2 UH, and IC features at 250 kPa, consistent with previous observations for Definity and other phospholipid encapsulated agents under unconfined conditions [84,85]. IC increased with pressure while the SHs and UHs became less prominent, and bubble disruption was evident from the decay of IC signals within successive pulses.

The spectral features were substantially different for the 100 and 200 μm channels, which are in the realm of the larger vessels of the microcirculation but outside the range that is typically associated with bioeffects for drug delivery and antivascular therapy [50,51]. There was a lack of clear and pronounced SH and UH peaks for the 0.1 ms pulses, although IC was evident starting at 500 kPa. The optical results indicate the prominent role of radiation forces: microbubbles are translated via

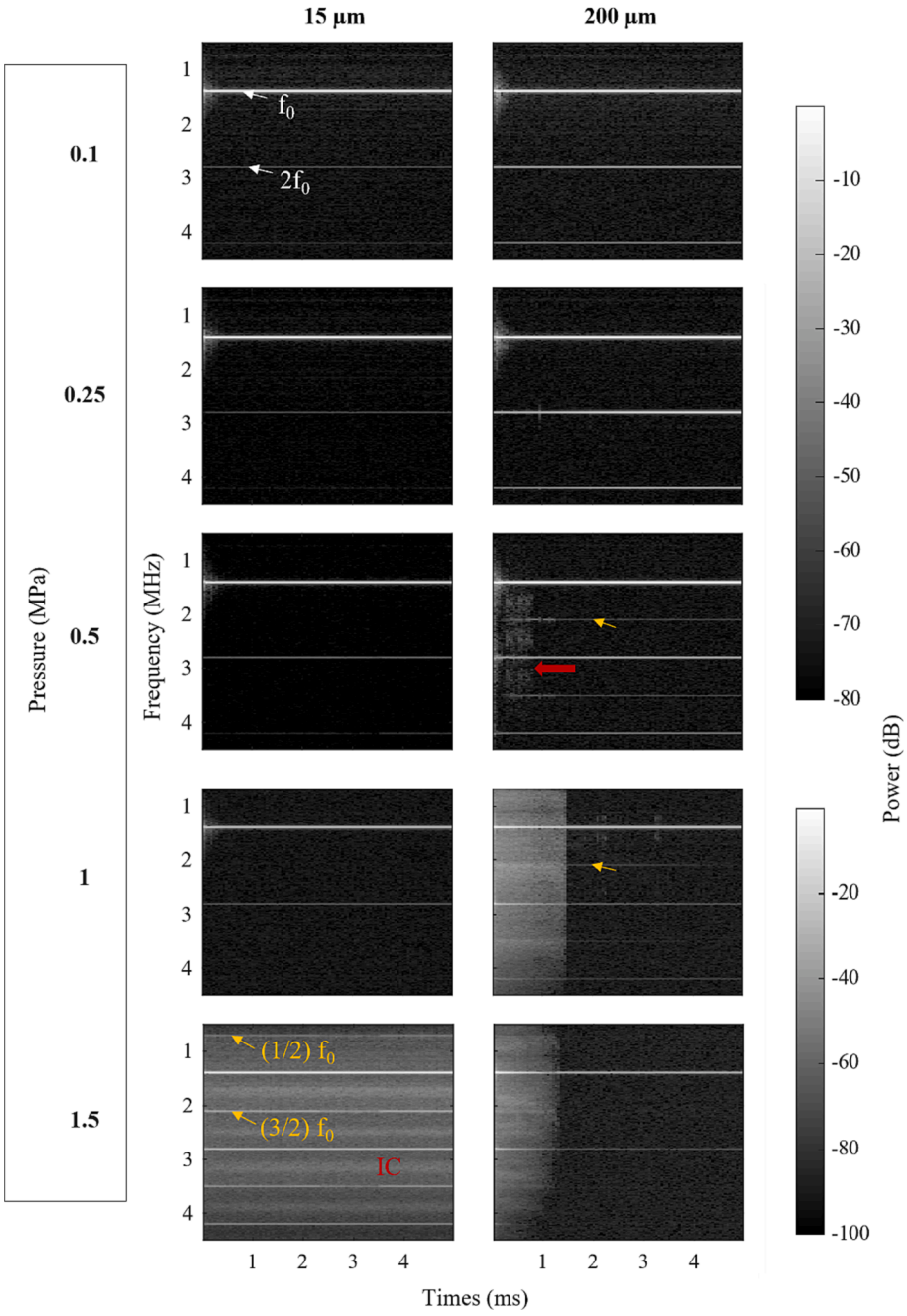

Fig. 12. Spectrograms of the cavitation signals from native Definity for the 5 ms pulsing scheme for different sonication pressures and channel diameters. White arrows point out fundamental f_0 and second harmonics $2f_0$. Yellow arrows indicate SHs and UHs and red arrows highlight areas with IC. (For interpretation of the references to colour in this figure legend, the reader is referred to the web version of this article.)

primary radiation forces to the distal wall with the vessel curvature facilitating the increased bubble density at mid-vessel depth where the optical focal plane is situated. The corresponding reduction in inter-bubble spacing can be expected to increase the role of secondary radiation forces, consistent with the formation of clusters observed along the distal wall at 2 and 3 MPa. The optical data support the disappearance of detected bubbles over time, concordant with the limited persistence of IC emissions. The 5 ms pulses in the 200 µm channels resulted in modest UHs at the 0.5–1 MPa range but were not evident at higher pressures. These latter results are broadly consistent with those previously reported by Chen *et al* [76] using high-speed imaging and emission detection in 200 µm diameter tubes for 5 ms pulses up to 1.5 MPa. They demonstrated the appearance of clustering against the distal wall and highlighted its potential role in influencing the evolution of cavitation spectra. There are differences in terms of the absence of SHs and UHs at 250 kPa for the 5 ms pulse which may be due to their use of cellulose hollow fiber and an in-house microbubble formulation rather than Definity. Optical evidence of radiation forces in small channels has also been reported in previous studies albeit in the absence of emissions detection and using shorter pulses [67–69,86].

The 50 µm diameter channel is within the upper size range of vessels that have shown to be impacted by antivascular therapy [22,50,87] and the results indicate that there is a transition in the spectral features [50]. In addition to a higher onset pressure for IC, there was the emergence of not only ‘conventional’ 1/2 SHs and 3/2 UHs, but more complex order SHs (2/3) and UHs (4/3, 5/3) at 2 and 3 MPa. Also notable in this vessel

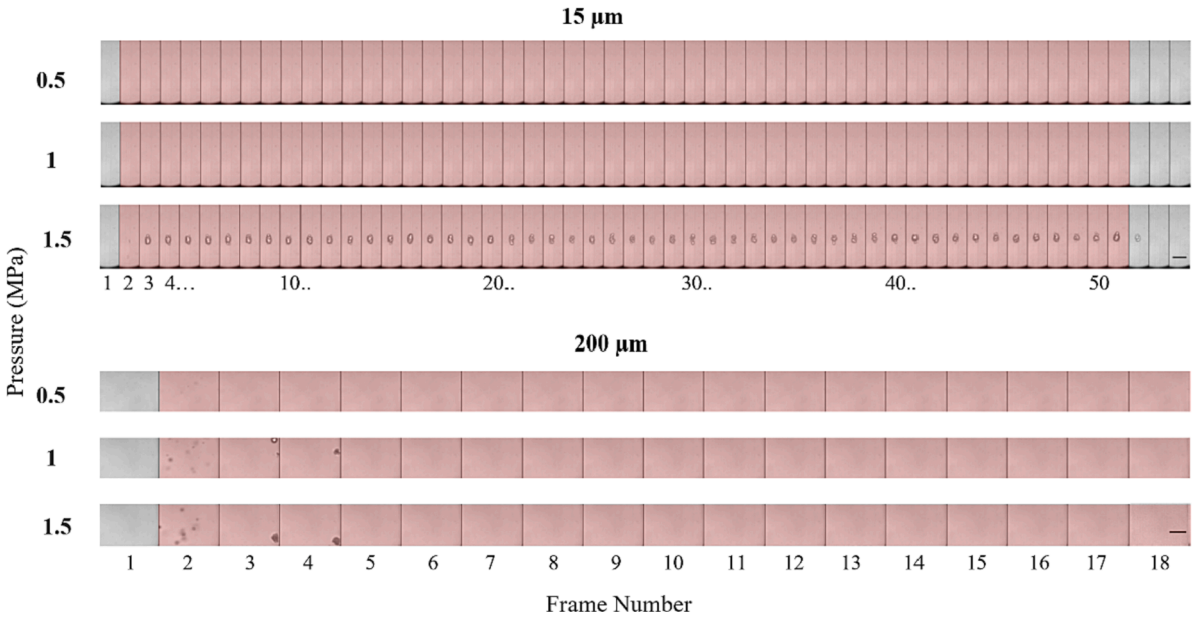

Fig. 13. Representative optical images from high-speed microscopy showing native Definity bubble activity during first burst of 5 ms pulsing scheme for different sonication pressures and channel diameters. Individual frames are delineated by vertical black lines and red shaded frames indicate frames acquired during ultrasound exposure. Channel boundaries are not indicated here due to scale, but can be seen in Fig. 10. Scale bars on the bottom rows represent 50 µm. (For interpretation of the references to colour in this figure legend, the reader is referred to the web version of this article.)

size was the increased persistence in emissions extended to the full 100 bursts. Optical results confirm the presence of bubble persistence and also indicate the presence of clusters at 2 and 3 MPa. Wall deformations adjacent to the clusters were also present on either side of the cluster, indicating the exertion of substantial forces by the clusters on the vessel walls. This is different from the 200 and 100 µm channels where the size of the clusters was smaller than the vessel dimension and they were situated along the distal wall, only held in place by radiation forces.

The 15 µm channel is directly within the size range of microvessels that are impacted in drug delivery [1–4] and antivascular therapy [21,22,50,87]. The spectral features continue to exhibit higher order SHs and UHs with IC at the higher pressures, along with a further increase in IC pressure threshold relative to the 50 µm channel case. The optical data indicate that, for 2 and 3 MPa, within each pulse there is a pattern of an initial expansion of individual bubbles, followed by clustering in the latter portion of the pulse. The timescale and resolution of the optical data do not permit further insight into this process, which may include the effect of secondary radiation forces, coalescence and fragmentation. At 2 MPa, the result is the formation of discrete clusters bounded by the (deformed) wall, whereas by 3 MPa the nature of the clustering can be described as elongated – essentially a dense bubble/cluster chain occupying a substantial fraction of the length of the channel. The transition between these two cases may relate to an increased number of smaller diameter bubbles undergoing substantial oscillation activity at the higher pressures (see below). At 3 MPa, scattering activity and visualized bubbles persisted over the full sequence of 0.1 ms pulses. The extended longevity of the bubbles in the smaller channel may relate to the influence of the channel wall resisting the collapse, fragmentation, and dissipation of bubbles. A trend of increased persistence in *ex vivo* vessels < 30 µm relative to within a 200 µm tube was observed previously for 2 cycle pulses at 2 MPa in [73]. For our 5 ms pulses, clustering was apparent by 1.5 MPa and persisted throughout the entire pulse. At the end of the pulse, damage was evident at the site of the clusters.

The trend of increased pressure threshold for IC onset with decreasing vessel diameter has been observed previously in work by Sassoroli *et al* [74,75] which experimentally examined this using emission detections from Optison populations at 2.02 and 1.736 MHz transmit frequencies in both rigid (silica and polyester tubes) and compliant (agar) channels ranging from 50 to 800 µm in diameter. This previous work was also supported by a theoretical analysis of gas-fluid coupling in a tube [88]. The results presented here are broadly consistent with this previous work and additionally extend the channel diameters assessed into the range most affected by drug delivery and antivascular ultrasound. It is also notable that these results are consistent with previous optical studies conducted in small rigid tubes in the 12–195 µm range that showed a reduced acoustic response of individual microbubble oscillations with decreasing vessel diameter during short ultrasound bursts [67]. These results are also supported by theoretical modeling of individual microbubbles within tubes [56,68,86,89].

Order 1/2 SH and 3/2 UH emissions from encapsulated microbubbles have received considerable attention in the biomedical ultrasound literature from experimental and theoretical perspectives due to their importance for imaging and therapeutic applications [39,84,90,91]. These are predicted with unencapsulated single bubble models and have been shown to occur at lower pressures and more readily in the case of phospholipid microbubble models due to the nonlinear response of the encapsulating shell [84,85,92,93]. Although the influence of how the vessel diameter will affect the SH and UH emissions of bubbles has not been reported, the results shown here are consistent with a decreasing channel diameter reducing the bubble oscillation amplitude and leading to an increased pressure threshold required for SH and UH emissions. The complex order SHs and UHs are not well reported with encapsulated biomedical microbubbles, and indeed appear only to have been observed anecdotally *in vivo* [31,32,35,46] and in a large channel agarose study [94] (discussed further below). For the case of volumetrically oscillating unencapsulated bubbles, higher order SHs and UHs are predicted to arise through instabilities and a progression through successive bifurcations [93,95]. In a recent study with encapsulated microbubbles, it was reported that a commonly used individual bubble model (Marmottant model [96]) predicted the occurrence of higher order SHs and UHs for a 25 MHz insonation frequency at relatively low pressure ranges (~0.25 MPa) for bubbles with resonant frequencies well below the driving frequency [97]. However, the optical data demonstrate that under conditions where complex order SHs and UHs occur, there are greatly expanded

bubble sizes that are closely spaced in conventional or elongated cluster configurations, which likely cannot be accounted for by individual bubble models that assume non-interaction, spherical symmetry, and relatively low oscillation amplitudes. In this regard, it is relevant to consider work in [98–100] which observed that when laser-induced bubble clouds (~500 μm in diameter) were insonated with pulsed ultrasound complex order SHs and UHs were initiated. The origin of these signatures was found to be periodic shock wave emissions associated with the cyclical growth and contraction of the clouds. In a subsequent study, periodic shock waves were also observed to arise from individual biomedical microbubbles that underwent fragmentation to create a bubble 'cloud' under exposure conditions relevant to therapeutic ultrasound, although only order 1/2 SHs were reported [66]. While the conditions reported in the present study are considerably more complex in that there is a confining environment and the starting point is a polydisperse population of pre-formed bubbles, it is possible that such cloud (or cluster) based behavior may be responsible for the complex order emissions. If this is the case, then in addition to the impact of bubble and cluster oscillation on microstreaming and possible jets and contact-based wall deformation, shock waves may also be a factor in eliciting bioeffects. It is also notable that in [94] order 1/3 SHs and UHs were observed to arise during exposures of microbubbles flowing through a 1.6 mm channel within agarose that was embedded with cells. Interestingly, this was reported at pressure levels ($\geq$0.76 MPa) that also induced the formation of microchannels by microbubbles that had penetrated the distal channel wall. While a mechanism for the complex order SHs and UHs was not established, the results of the present study raise the possibility that they may be associated with the subset of microbubbles that were present within the microchannels.

Indeed, observations of wall damage in the 15 μm channel were spatially associated with the presence of clusters that induced deformations on the channel wall. The limited temporal resolution of the camera was insufficient to establish if the periodic oscillations clusters observed in [98–100] in unconstrained conditions were also present in the 15 μm channel. It is however notable that complex order SHs and UHs were present that would be consistent with this occurring. These observations and the potential role of cluster behavior in vessel damage at higher pressures suggest that this warrants further investigation with a higher temporal resolution and in terms of the potential for shock wave generation. It is also notable that the 5 ms pulse achieved damage at a lower pressure than the short pulse sequence (1.5 versus 3 MPa) and with less than half the total insonation time (10.2 ms for the 100 bursts short pulse sequence). In both the short and long pulse cases, SHs, UHs, and IC were present for the duration of insonation. Based on the optical observations, a contributing factor to the reduced damage of the shorter pulse may be that for the initial portion of the on-time for each pulse the expanded bubbles were spatially diffuse before clustering in the latter portion of the pulse. This is in contrast to the 5 ms case where once formed, sustained cluster activity was present for the pulse duration. Interestingly, the 200 μm channel was not damaged by either pulse type. The inability to elicit damage in the larger channel may be due to the differences in the nature of bubble and cluster oscillations when they are present at a boundary. The reduced capacity to initiate damage in the 200 μm channel may also be due to bubbles and clusters only being held in contact at the wall with radiation forces. This is in contrast to the small channel, where clusters are on the order of the channel sizes and are constrained, which may facilitate the exertion of larger forces. Microbubble mediated damage of agarose has been previously reported in [101] and [94] where it was shown that with sustained pulsing, microbubbles could penetrate into the walls of 230 and 1600 μm channels leaving behind patent tunnels. The absence of detected damage in the present study for the 200 μm case is attributed to one pulse being sent whereas hundreds of 10 ms pulses were transmitted in [94] and [101], which presumably accumulated damage and modification of the channel wall that ultimately permitted tunnel development. Notably, the threshold for tunnel formation at 1 MHz in [101] was found to be 1.5 MPa for the 10 ms case, similar to that observed here at 1.4 MHz with 5 ms pulses for the 15 μm channel.

While native Definity is a widely employed agent in therapeutic ultrasound, the filtered Definity results are of interest from two main perspectives. First, they provide insight into the role of a smaller subpopulation of bubbles in the results for native Definity. Second, they are effectively an example of a nanobubble agent, which is a topic of increasing interest in biomedical ultrasound. In terms of the former point, it should be noted that while the bulk of the volume fraction of Definity is comprised of bubbles with diameters $>$ 1 μm, it is bubbles $<$1 μm that account for the bulk of the number density [82,102,103]. While phospholipid encapsulated bubbles in this size range will have a resonance frequency far above the transmit frequency employed, it has been shown that at sufficiently high pressures they will reach a threshold that they will undergo expansion-dominated oscillations – effectively acting as cavitation 'seeds' [83]. For example, in [83], by 1 MPa a population of $<$ 0.4 μm nanobubbles had similar scattering strength and emissions as microbubbles (number distribution mode 0.21 μm, volume distribution mode 3.9 μm) for the same number density. This is consistent with the filtered Definity exhibiting broadly similar optical characteristics and emission spectra as native Definity for the 2 and 3 MPa cases. This supports that a population of smaller bubbles (not just restricted to $<$ 0.45 μm) present within Definity may be playing a significant role in the behavior of native Definity at higher pressures. With regard to the use of nanobubble formulations for therapy, there have been recent reports for drug delivery [104,105] and antivascular therapy [106]. One rationale applicable to both cases is that nanobubbles afford a higher number density to be present within the vasculature, possibly with a more homogenous response than polydisperse agents that include larger bubbles. An additional rationale [106] is that their higher threshold for IC may be advantageous in confining the intended bioeffects to the focal region of the transducer beam as a strategy to mitigate unintended prefocal bioeffects. With regard to their use in an antivascular exposure regime, it is notable that channel damage was observed in the 15 μm case for native but not filtered Definity. One contributing factor may be the higher IC threshold relative to native Definity. A second may be the higher number density (18x native Definity for the 0.5x volume fraction employed) which in turn may result in cluster behavior that has a reduced capacity to elicit a damaging effect. In [98], it was found, at least for the case of a 230 μm channel, that higher number concentrations of a microbubble agent resulted in a reduced level of tunneling into the channel wall. This suggests that the concentration of nanobubble agents in this setting warrants investigation.

It is useful to consider these results in the context of *in vivo* work that has been done to date. For antivascular therapy, there has been a wide range of exposure conditions and agent concentrations employed [5,7,50,107]. There is however considerable evidence accumulated that acute perfusion shutdown can begin to be achieved with pressure levels that exceed 1 MPa and that by 3 MPa a substantial vascular shutdown can occur when longer pulses are employed ($>$0.1 ms) [50,108,109]. In our previous work in tumors with the 0.1 ms pulse sequence, profound therapeutically relevant vascular shutdown occurred with a pulse that has 1.6 MPa peak negative and 3.5 MPa peak positive pressure [31,32,35,106]. The pulse asymmetry was due to nonlinear propagation as a loosely focused transducer was employed to enable full tumor spatial coverage. In [50] 5 ms pulses were examined at 1, 2, and 3 MPa in tumour vessels. At 1 MPa, there was minimal vascular damage, however this increased rapidly with pressure at 2 and then 3 MPa, beginning with smaller ($<$20 μm) vessels preferentially and then expanding to include larger ones (up to 71 μm). The present results show that this transition to 2 and 3 MPa increased bubble activity. It is also notable that in [50] microvascular damage leading to blood flow disruption was observed to be initiated at focal points using 5 ms pulses at 2 and 3 MPa. Previous studies have also linked optical evidence of short pulse (1–2 cycles) induced bubble behavior (expansions, jets) to localized vascular wall damage of capillary sized vessels in ex vivo tissue

preparations [70,73,110].

The results have implications for the interpretation and use of cavitation spectra in microbubble-mediated FUS. In this setting, emissions spectra that are reported and used for control purposes are invariably derived from relatively large volumes defined by the overlap between the therapy beam focal region and the passive cavitation detector - either one or more elements, or increasingly the array-based beamformed region of interest [39]. Typically, this region is many cubic millimeters in size and as such it will necessarily encompass a wide range of microvessel diameters and also smaller arteries and veins. Even if the arteries and veins are excluded, the majority of the blood volume fraction contained within the microvasculature resides within its larger vessels [52,53,111]. If as a first order approximation it is assumed that the emissions from microbubbles within each vessel type are proportional to its volume of blood, then only a fraction of the received signals used for control will arise from the smaller microvessels, which are the effective target of the therapy. While it has long been recognized that the behavior of microbubbles in the smallest vessels will be different from an unconfined state, the results here indicate that the emissions arising from these vessels can be distinctly different from the larger microvessels in terms of spectral characteristics and persistence.

The body of work for cavitation control has established, based on bulk signals, a correlation of emissions with bioeffects. The present work highlights that the signals from bulk emissions - containing a wide range of vessel calibers - may not necessarily provide an indication of the emissions within the target vessels of the therapy, as these may only be a small contributor to the net signal. The present results do not in any way invalidate this work but do suggest that caution should be used in concluding that the bulk signal characteristics provide an indication of what the emission characteristics are within the target vessels.

As an example, the emissions characteristics for antivascular therapy have been poorly examined to date, but anecdotal bulk emissions from tumors have been reported, where small peaks at the 1/3 and 2/3 SHs and 4/3 and 5/3 UHs can be observed. However in [50] which assesses cavitation in a microvascular bed that excludes larger vessels, these signals are present more prominently, consistent with the phantom results for smaller vessels.

The phantom results therefore further support the value of the considerable work that is ongoing to derive super-resolution microvascular maps in the setting of therapeutic ultrasound [112–115]. In particular, the data suggest that it would be valuable to map specific signatures present in small vessels that are associated with bioeffects. For example in the setting of antivascular therapy this may be complex order SHs and UHs. In the setting of bulk emissions in the absence of applying super resolution methods, the present data suggest investigating the use of not only the distinct spectral signatures but also the temporal characteristics of signatures within the transmit pulses to take advantage of the apparently increased persistence of bubbles and their emissions within the smallest vessels.

5. Limitations

This study has a number of notable limitations. One is that in general microbubbles were not optically observable until they were undergoing sufficiently substantial oscillations, which tended to happen only at the larger pressure levels $\geq$ 0.5 MPa. A primary factor influencing this is that bubbles were necessarily situated throughout the channel and the large majority were not in the optical focal plane prior to the initiation of exposures. This is in contrast to many previous high-speed optical imaging studies where microbubbles were floated to the surface of a chamber membrane or channel [116], or in a smaller number of studies offset from a boundary with optical tweezers [117–119]. In the present study, bubble visualization was facilitated by both the expansion of bubbles upon exposure and their translation and concentration along the distal mid-line of the channels which was within the optical focal plane. In addition to optical observation challenges, lower pressures also presented challenges in terms of signal to noise ratio in the smallest channels. Collectively this imposed limitations on the ability to provide insight into behaviors at traditional drug delivery pressures (<1 MPa).

There were also significant limitations imposed by the temporal resolution. One aspect of this was the exposure time for a given frame (1 μs), which is on the order of a single insonation cycle and therefore resulted in a blurring of bubbles and inhibited the ability to visualize bubble boundaries or transient events (e.g. jets) at points in time. A second impact was that while the camera enabled the observation of longer time scale bubble events, its frame rate was insufficient to temporally track cyclical oscillations or rapid transient events. Cameras with Mframes/s capacity can capture such events, but suffer from limitations in terms of the number of frames and therefore total duration that can be recorded. Notably, the work of Chen *et al* [120] overcame this by employing a dual camera system to observe in a 200 μm channel both millisecond timescale and shorter duration 25 Mframes/s imaging. The results obtained here for the smaller channels, in particular the clustering events that appear to be associated with complex order SHs and UHs, suggest that such an approach should be pursued in future work.

It is also notable that the channels were bounded by agarose, which although arguably more relevant to *in vivo* conditions in terms of mechanical properties than rigid channels that were previously employed [65,67,69,76], it does not fully recapitulate the mechanical properties of microvascular walls surrounded by an extravascular space. Further, the longer pulses resulted in damage to the walls before the full pressure range could be executed. Conducting experiments with other compliant materials is therefore also warranted to gain insight into the effects of mechanical properties on the observed results. Although the present study appears to have employed the smallest compliant channels to date (12 μm rigid tubes employed previously [67]), attempts to approach the size of human capillaries (8–10 μm) warrant further effort. In these experiments, the use of dyes to better demarcate channel walls would permit a more detailed identification of potential damage.

Considerable efforts were made to reduce the length of the smallest portion of the channels and to employ low flow rates (along with incorporating a proximal line flush outlet) as it has previously been reported that flowing through small gauge syringes at higher speeds can modify bubble populations [121]. The possible impact of the procedures on bubble populations was assessed with Coulter Counter measurements (Supplemental Fig. 2 and Table 1). Population changes were detected as relatively small shifts in concentration and mean size for 100 μm, which were more pronounced by 50 μm. A Coulter Counter was not possible to employ for the 15 μm channel due to collection volume limitations, but an optical sizing experiment indicated that larger bubbles remained present (Supplementary Fig. 15) [122]. As a relative amplitude comparison was not performed between the channels, this does not impact the nature of the conclusions made in the study. Further, as similar features of emissions and optical data were obtained for the native and filtered Definity populations at higher pressures, this suggests that at least at higher pressures, these effects do not impact the main findings of the paper.

6. Conclusion

Microbubble based FUS approaches are undergoing rapid development in terms of basic preclinical research, technical developments, and an increasing number of clinical trials. The successful clinical translation of these methods hinges in large part upon understanding the links between bioeffects and cavitation, in addition to developing and refining methods to exploit this knowledge for control purposes. The dominant approaches involve employing emissions derived from relatively large sample volumes containing a wide range of vessel calibers, where only a fraction of the emissions are derived from target therapy vessels. The results of the present study suggest that the behaviors and emissions of the bubbles situated in channels with diameters similar to microvessels

impacted by therapy are distinctly different from larger channels. Radiation forces and clustering appear to play a central role in bubble behavior under these conditions. The results have implications for the development of control and imaging methods that exploit these signatures.

Declaration of Competing Interest

The authors declare that they have no known competing financial interests or personal relationships that could have appeared to influence the work reported in this paper.

Acknowledgments

The authors would like to thank Carly Pellow for her assistance with the Coulter Counter measurements, Michael Pozzobon for machining the transducer holder and phantom chambers used in this work, Marc Santos and Chris Acconcia for their helpful insights, Kang Huang for his design of the website to visualize optical images, and Carly Pellow, Rojin Anbarafshan and Amin Sojahrood for discussions and manuscript review. This work was supported by the Canadian Institutes of Health Research (PJT 156131) and the Ontario Research Fund (RE08-020).

Appendix A. Supplementary data

Supplementary data to this article can be found online at https://doi.org/10.1016/j.ultsonch.2023.106291.

References

[1] S.M. Stieger, C.F. Caskey, R.H. Adamson, S. Qin, F.E. Curry, E.R. Wisner, K. W. Ferrara, Enhancement of vascular permeability with low-frequency contrast-enhanced ultrasound in the chorioallantoic membrane model, Radiology 243 (1) (2007) 112–121.

[2] E.E. Cho, J. Drazic, M. Ganguly, B. Stefanovic, K. Hynynen, Two-photon fluorescence microscopy study of cerebrovascular dynamics in ultrasound-induced blood—brain barrier opening, J. Cereb. Blood Flow Metab. 31 (9) (2011) 1852–1862.

[3] T. Nhan, A. Burgess, E.E. Cho, B. Stefanovic, L. Lilge, K. Hynynen, Drug delivery to the brain by focused ultrasound induced blood–brain barrier disruption: Quantitative evaluation of enhanced permeability of cerebral vasculature using two-photon microscopy, Available, J. Control. Release 172 (1) (2013) 274–280, http://www.sciencedirect.com.myaccess.library.utoronto.ca/science/article/pii/S0168365913004987.

[4] A. Burgess, T. Nhan, C. Moffatt, A.L. Klibanov, K. Hynynen, Analysis of focused ultrasound-induced blood–brain barrier permeability in a mouse model of Alzheimer's disease using two-photon microscopy, Available, J. Control. Release 192 (2014) 243–248, http://www.sciencedirect.com.myaccess.library.utoronto.ca/science/article/pii/S0168365914005628.

[5] D.E. Goertz, An overview of the influence of therapeutic ultrasound exposures on the vasculature: High intensity ultrasound and microbubble-mediated bioeffects, Int. J. Hyperth. 31 (2) (2015.) 134–144.

[6] P. Qin, T. Han, A.C.H. Yu, L. Xu, Mechanistic understanding the bioeffects of ultrasound-driven microbubbles to enhance macromolecule delivery, Available, J. Controlled Release 272 (2018) 169–181, https://www.sciencedirect.com/science/article/pii/S0168365918300026.

[7] K. Kooiman, S. Roovers, S.A. Langeveld, R.T. Kleven, H. Dewitte, M.A. O'Reilly, J. Escoffre, A. Bouakaz, M.D. Verweij, K. Hynynen, Ultrasound-responsive cavitation nuclei for therapy and drug delivery, Ultrasound Med. Biol. 46 (6) (2020) 1296–1325.

[8] Y. Meng, Z. Shirzadi, B. MacIntosh, C. Heyn, G. S. Smith, I. Aubert, C. Hamani, S. Black, K. Hynynen and N. Lipsman, Blood-brain barrier opening in Alzheimer's disease using MR-guided focused ultrasound, Neurosurgery, vol. 66, (Supplement_1), pp. nyz310_208, 2019.

[9] T. Mainprize, N. Lipsman, Y. Huang, Y. Meng, A. Bethune, S. Ironside, C. Heyn, R. Alkins, M. Trudeau, A. Sahgal, Blood-brain barrier opening in primary brain tumors with non-invasive MR-guided focused ultrasound: a clinical safety and feasibility study, Sci. Rep. 9 (1) (2019) 1–7.

[10] A. Abrahao, Y. Meng, M. Llinas, Y. Huang, C. Hamani, T. Mainprize, I. Aubert, C. Heyn, S.E. Black, K. Hynynen, First-in-human trial of blood–brain barrier opening in amyotrophic lateral sclerosis using MR-guided focused ultrasound, Nat. Commun. 10 (1) (2019) 1–9.

[11] R.M. Bunte, S. Ansaloni, C.M. Sehgal, W.M.F. Lee, A.K.W. Wood, Histopathological observations of the antivascular effects of physiotherapy ultrasound on a murine neoplasm, Ultrasound Med. Biol. 32 (3) (2006) 453–461.

[12] A.K. Wood, S. Ansaloni, L.S. Ziemer, W.M. Lee, M.D. Feldman, C.M. Sehgal, The antivascular action of physiotherapy ultrasound on murine tumors, Ultrasound Med. Biol. 31 (10) (2005) 1403–1410.

[13] D.L. Miller, Overview of experimental studies of biological effects of medical ultrasound caused by gas body activation and inertial cavitation, Available, Prog. Biophys. Mol. Biol. 93 (1) (2007) 314–330, http://www.sciencedirect.com/science/article/pii/S0079610706000976.

[14] N. McDannold, Y. Zhang, C. Power, F. Jolesz, N. Vykhodtseva, Nonthermal ablation with microbubble-enhanced focused ultrasound close to the optic tract without affecting nerve function, J. Neurosurg. 119 (5) (2013) 1208–1220.

[15] C.D. Arvanitis, N. Vykhodtseva, F. Jolesz, M. Livingstone, N. McDannold, Cavitation-enhanced nonthermal ablation in deep brain targets: feasibility in a large animal model, J. Neurosurg. 124 (5) (2016) 1450–1459.

[16] A.K.W. Wood, The antivascular action of physiotherapy ultrasound on a murine tumor: role of a microbubble contrast agent, Ultrasound Med. Biol. 33 (12) (2007) 1901–1910.

[17] D. E. Goertz, R. Karshafian, K. Hynynen, Antivascular effects of pulsed low intensity ultrasound and microbubbles in mouse tumors, in: 2008 IEEE Ultrasonics Symposium, 2008, pp. 670-673.

[18] Y. Ho, Y. Chang, C. Yeh, Improving nanoparticle penetration in tumors by vascular disruption with acoustic droplet vaporization, Theranostics 6 (3) (2016) 392–403.

[19] L.G. Daenen, Y. Shaked, S. Man, P. Xu, E.E. Voest, R.M. Hoffman, D.J. Chaplin, R. S. Kerbel, Low-dose metronomic cyclophosphamide combined with vascular disrupting therapy induces potent antitumor activity in preclinical human tumor xenograft models, Mol. Cancer. Ther. 8 (10) (2009) 2872–2881.

[20] Z. Liu, S. Gao, Y. Zhao, P. Li, J. Liu, P. Li, K. Tan, F. Xie, Disruption of tumor neovasculature by microbubble enhanced ultrasound: a potential new physical therapy of anti-angiogenesis, Ultrasound Med. Biol. 38 (2) (2012) 253–261.

[21] Y. Ho, T. Wang, C. Fan, C. Yeh, Current progress in antivascular tumor therapy, Drug Discov. Today 22 (10) (2017) 1503–1515.

[22] Y. Ho, T. Wang, C. Fan, C. Yeh, Spatially uniform tumor treatment and drug penetration by regulating ultrasound with microbubbles, ACS Appl. Mater. Interfaces vol. 10(21) (May 30, 2018.) 17784–17791.

[23] R.M. Jones, D. McMahon, K. Hynynen, Ultrafast three-dimensional microbubble imaging in vivo predicts tissue damage volume distributions during nonthermal brain ablation, Theranostics 10 (16) (2020) 7211–7230.

[24] A.K.W. Wood, Antivascular ultrasound therapy extends survival of mice with implanted melanomas, Ultrasound Med. Biol. 36 (5) (2010) 853–857.

[25] C.W. Burke, A.L. Klibanov, J.P. Sheehan, R.J. Price, Inhibition of glioma growth by microbubble activation in a subcutaneous model using low duty cycle ultrasound without significant heating, J. Neurosurg. 114 (6) (2011) 1654–1661.

[26] Z. Shen, G. Xia, M. Wu, M. Shi, F. Qiang, E. Shen, B. Hu, The effects of low-frequency ultrasound and microbubbles on rabbit hepatic tumors, Exp. Biol. Med. 239 (6) (2014) 747–757.

[27] G.J. Czarnota, R. Karshafian, P.N. Burns, S. Wong, A. Al Mahrouki, J.W. Lee, A. Caissie, W. Tran, C. Kim, M. Furukawa, "Tumor radiation response enhancement by acoustical stimulation of the vasculature," Proceedings of the National Academy of Sciences, vol. 109, (30), pp. E2033-E2041, 2012.

[28] A.A. Al-Mahrouki, S. Iradji, W.T. Tran, G.J. Czarnota, Cellular characterization of ultrasound-stimulated microbubble radiation enhancement in a prostate cancer xenograft model, Dis. Model. Mech. 7 (3) (2014) 363–372.

[29] P. Lai, C. Tarapacki, W.T. Tran, A. El Kaffas, J. Lee, C. Hupple, S. Iradji, A. Giles, A. Al-Mahrouki, G.J. Czarnota, Breast tumor response to ultrasound mediated excitation of microbubbles and radiation therapy in vivo, Oncoscience 3 (3–4) (2016) 98–108.

[30] A. Daecher, M. Stanczak, J. Liu, J. Zhang, S. Du, F. Forsberg, D.B. Leeper, J. R. Eisenbrey, Localized microbubble cavitation-based antivascular therapy for improving HCC treatment response to radiotherapy, Cancer Lett. 411 (2017) 100–105.

[31] D.E. Goertz, M. Todorova, O. Mortazavi, V. Agache, B. Chen, R. Karshafian, Antitumor effects of combining docetaxel (taxotere) with the antivascular action of ultrasound stimulated microbubbles. PLoS ONE, vol. 7, (12), 2012.

[32] M. Todorova, V. Agache, O. Mortazavi, B. Chen, R. Karshafian, K. Hynynen, S. Man, R.S. Kerbel, D.E. Goertz, Antitumor effects of combining metronomic chemotherapy with the antivascular action of ultrasound stimulated microbubbles, Int. J. Cancer 132 (12) (2013) 2956–2966.

[33] Y. Jing, Z. Xiu-Juan, C. Hong-Jiao, C. Zhi-Kui, Q. Qing-Fu, X. En-Sheng, L. Li-Wu, Ultrasound-targeted microbubble destruction improved the antiangiogenic effect of Endostar in triple-negative breast carcinoma xenografts, J. Cancer Res. Clin. Oncol. 145 (5) (2019) 1191–1200.

[34] S.J. Hunt, T. Gade, M.C. Soulen, S. Pickup, C.M. Sehgal, Antivascular ultrasound therapy: magnetic resonance imaging validation and activation of the immune response in murine melanoma, J. Ultrasound Med. 34 (2) (2015) 275–287.

[35] S. Bulner, A. Prodeus, J. Gariepy, K. Hynynen, D.E. Goertz, Enhancing checkpoint inhibitor therapy with ultrasound stimulated microbubbles, Ultrasound Med. Biol. 45 (2) (2019) 500–512.

[36] N. McDannold, N. Vykhodtseva, K. Hynynen, Targeted disruption of the blood–brain barrier with focused ultrasound: association with cavitation activity, Phys. Med. Biol. 51 (4) (2006) 793–807.

[37] Y. Tung, F. Vlachos, J.J. Choi, T. Deffieux, K. Selert, E.E. Konofagou, In vivo transcranial cavitation threshold detection during ultrasound-induced blood-brain barrier opening in mice, Phys. Med. Biol. 55 (20) (2010) 6141–6155.

[38] M.A. O'Reilly, K. Hynynen, A PVDF receiver for ultrasound monitoring of transcranial focused ultrasound therapy, IEEE Trans. Biomed. Eng. 57 (9) (2010) 2286–2294.

[39] M.A. O'Reilly, K. Hynynen, Blood-brain barrier: real-time feedback-controlled focused ultrasound disruption by using an acoustic emissions–based controller, Radiology 263 (1) (2012) 96–106.

[40] C. Bing, Characterization of different bubble formulations for blood-brain barrier opening using a focused ultrasound system with acoustic feedback control, Sci. Rep. vol. 8, (1) (2018) 7986.

[41] C. Tsai, J. Zhang, Y. Liao, H. Liu, Real-time monitoring of focused ultrasound blood-brain barrier opening via subharmonic acoustic emission detection: implementation of confocal dual-frequency piezoelectric transducers, Phys. Med. Biol. 61 (7) (2016) 2926–2946.

[42] C.D. Arvanitis, M.S. Livingstone, N. Vykhodtseva, N. McDannold, Controlled ultrasound-induced blood-brain barrier disruption using passive acoustic emissions monitoring, PLoS One 7 (9) (2012) e45783.

[43] T. Sun, Y. Zhang, C. Power, P. M. Alexander, J. T. Sutton, M. Aryal, N. Vykhodtseva, E. L. Miller, N. J. McDannold, Closed-loop control of targeted ultrasound drug delivery across the blood-brain/tumor barriers in a rat glioma model, Proc. Natl. Acad. Sci. U. S. A., vol. 114, (48), pp. E10281-E10290, November 28, 2017.

[44] H.A. Kamimura, J. Flament, J. Valette, A. Cafarelli, R. Aron Badin, P. Hantraye, B. Larrat, Feedback control of microbubble cavitation for ultrasound-mediated blood–brain barrier disruption in non-human primates under magnetic resonance guidance, J. Cereb. Blood Flow Metab. 39 (7) (2019) 1191–1203.

[45] D.E. Goertz, R. Karshafian, K. Hynynen, Investigating the effects of pulsed low intensity ultrasound and microbubbles in mouse tumors, in 2009 IEEE International Ultrasonics Symposium, 2009, pp. 89-92.

[46] M.A. Santos, S. Wu, Z. Li, D.E. Goertz, K. Hynynen, Microbubble-assisted MRI-guided focused ultrasound for hyperthermia at reduced power levels, vol. 35, (1), pp. 599-611, December 31, 2018.

[47] J.H. Hwang, J. Tu, A.A. Brayman, T.J. Matula, L.A. Crum, Correlation between inertial cavitation dose and endothelial cell damage in vivo, Ultrasound Med. Biol. 32 (10) (2006) 1611–1619.

[48] C.R. Jensen, R.W. Ritchie, M. Gyöngy, J.R. Collin, T. Leslie, C. Coussios, Spatiotemporal monitoring of high-intensity focused ultrasound therapy with passive acoustic mapping, Radiology 262 (1) (2012) 252–261.

[49] P. Huang, X. You, M. Pan, S. Li, Y. Zhang, Y. Zhao, M. Wang, Y. Hong, Z. Pu, L. Chen, A novel therapeutic strategy using ultrasound mediated microbubbles destruction to treat colon cancer in a mouse model, Cancer Lett. 335 (1) (2013) 183–190.

[50] X. Zhao, C. Pellow, D.E. Goertz, Intravital imaging and cavitation monitoring of antivascular ultrasound in tumor microvasculature, Theranostics 13 (1) (2023) 250–266.

[51] S.B. Raymond, J. Skoch, K. Hynynen, B.J. Bacskai, Multiphoton Imaging of Ultrasound/Optison Mediated Cerebrovascular Effects in vivo, J. Cereb. Blood Flow Metab. 27 (2) (2007) 393–403.

[52] C. Kirst, S. Skriabine, A. Vieites-Prado, T. Topilko, P. Bertin, G. Gerschenfeld, F. Verny, P. Topilko, N. Michalski, M. Tessier-Lavigne, N. Renier, Mapping the fine-scale organization and plasticity of the brain vasculature, Available, Cell 180 (4) (2020) 780–795.e25, https://www.sciencedirect.com/science/article/pii/S0092867420301094.

[53] M.I. Townsley, Structure and composition of pulmonary arteries, capillaries, and veins, Compr. Physiol., vol. 2, (1), pp. 675-709, January 01, 2012.

[54] E. Sassaroli, K. Hynynen, Forced linear oscillations of microbubbles in blood capillaries, J. Acoust. Soc. Am. 115 (6) (2004) 3235–3243.

[55] E. Sassaroli, K. Hynynen, Resonance frequency of microbubbles in small blood vessels: a numerical study, Phys. Med. Biol. 50 (22) (2005) 5293.

[56] S. Qin, K.W. Ferrara, Acoustic response of compliable microvessels containing ultrasound contrast agents, Phys. Med. Biol. 51 (20) (2006) 5065.

[57] S. Qin, K.W. Ferrara, The natural frequency of nonlinear oscillation of ultrasound contrast agents in microvessels, Ultrasound Med. Biol. 33 (7) (2007) 1140–1148.

[58] N. Hosseinkhah, K. Hynynen, A three-dimensional model of an ultrasound contrast agent gas bubble and its mechanical effects on microvessels, Phys. Med. Biol. 57 (3) (2012) 785.

[59] N. Hosseinkhah, H. Chen, T. Matula, P. Burns, K. Hynynen, Mechanisms of microbubble–vessel interactions and induced stresses: a numerical study, J. Acoust. Soc. Am. 134 (3) (2013) 1875–1885.

[60] B. Helfield, X. Chen, S.C. Watkins, F.S. Villanueva, Biophysical insight into mechanisms of sonoporation, Proc. Natl. Acad. Sci. 113 (36) (2016) 9983–9988.

[61] P. Prentice, A. Cuschieri, K. Dholakia, M. Prausnitz, P. Campbell, Membrane disruption by optically controlled microbubble cavitation, Nat. Phys. 1 (2) (2005) 107–110.

[62] G. Renaud, J.G. Bosch, A.F. Van Der Steen, N. De Jong, Low-amplitude non-linear volume vibrations of single microbubbles measured with an "acoustical camera", Ultrasound Med. Biol. 40 (6) (2014) 1282–1295.

[63] N. De Jong, M. Emmer, A. Van Wamel, M. Versluis, Ultrasonic characterization of ultrasound contrast agents, Med. Biol. Eng. Comput. 47 (8) (2009) 861–873.

[64] N. de Jong, P.J. Frinking, A. Bouakaz, M. Goorden, T. Schourmans, X. Jingping, F. Mastik, Optical imaging of contrast agent microbubbles in an ultrasound field with a 100-MHz camera, Ultrasound Med. Biol. 26 (3) (2000) 487–492.

[65] S. Cleve, C. Inserra, P. Prentice, Contrast agent microbubble jetting during initial interaction with 200-kHz focused ultrasound, Ultrasound Med. Biol. 45 (11) (2019) 3075–3080.

[66] J.H. Song, A. Moldovan, P. Prentice, Non-linear acoustic emissions from therapeutically driven contrast agent microbubbles, Ultrasound Med. Biol. 45 (8) (2019) 2188–2204.

[67] C.F. Caskey, D.E. Kruse, P.A. Dayton, T.K. Kitano, K.W. Ferrara, Microbubble oscillation in tubes with diameters of 12, 25, and 195 microns, Appl. Phys. Lett. 88 (3) (2006), 033902.

[68] H. Zheng, P.A. Dayton, C. Caskey, S. Zhao, S. Qin, K.W. Ferrara, Ultrasound-driven microbubble oscillation and translation within small phantom vessels, Ultrasound Med. Biol. 33 (12) (2007) 1978–1987.

[69] D.H. Thomas, V. Sboros, M. Emmer, H. Vos, N. De Jong, Microbubble oscillations in capillary tubes, IEEE Trans. Ultrason. Ferroelectr. Freq. Control 60 (2013) (1).

[70] H. Chen, A. Brayman, M. Bailey, T. Matula, Blood vessel rupture by cavitation, Urol. Res. 38 (4) (2010) 321–326.

[71] H. Chen, W. Kreider, A.A. Brayman, M.R. Bailey, T.J. Matula, Blood vessel deformations on microsecond time scales by ultrasonic cavitation, Phys. Rev. Lett. 106 (2011) (3).

[72] H. Chen, A.A. Brayman, W. Kreider, M.R. Bailey, T.J. Matula, Observations of translation and jetting of ultrasound-activated microbubbles in mesenteric microvessels, Ultrasound Med. Biol. 37 (12) (2011) 2139–2148.

[73] C.F. Caskey, S.M. Stieger, S. Qin, P.A. Dayton, K.W. Ferrara, Direct observations of ultrasound microbubble contrast agent interaction with the microvessel wall, J. Acoust. Soc. Am. 122 (2) (2007) 1191–1200.

[74] E. Sassaroli, K. Hynynen, On the impact of vessel size on the threshold of bubble collapse, Appl. Phys. Lett. 89 (12) (2006), 123901.

[75] E. Sassaroli, K. Hynynen, Cavitation threshold of microbubbles in gel tunnels by focused ultrasound, Ultrasound Med. Biol. 33 (10) (2007) 1651–1660.

[76] X. Chen, J. Wang, J.J. Pacella, F.S. Villanueva, Dynamic behavior of microbubbles during long ultrasound tone-burst excitation: mechanistic insights into ultrasound-microbubble mediated therapeutics using high-speed imaging and cavitation detection, Ultrasound Med. Biol. 42 (2) (2016) 528–538.

[77] J.H. Song, P. Prentice, Spectral peak suppression in the acoustic emissions from multiple microbubbles cavitating in focused ultrasound, in - 2019 IEEE International Ultrasonics Symposium (IUS), 2019, pp. 2283-2286.

[78] C. Poon, D. McMahon, K. Hynynen, Noninvasive and targeted delivery of therapeutics to the brain using focused ultrasound, Neuropharmacology 120 (2017) 20–37.

[79] K. Kooiman, H.J. Vos, M. Versluis, N. de Jong, Acoustic behavior of microbubbles and implications for drug delivery, Available, Adv. Drug Deliv. Rev. 72 (2014) 28–48, http://www.sciencedirect.com/science/article/pii/S0169409X14000374.

[80] S. V. Morse, A. N. Pouliopoulos, T. G. Chan, M. J. Copping, J. Lin, N. J. Long, J. J. Choi, Rapid short-pulse ultrasound delivers drugs uniformly across the murine blood-brain barrier with negligible disruption, Radiology, vol. 291, (2), pp. 459-466, May 01, 2019.

[81] S.P. Fletcher, M. Choi, R. Ramesh, M.A. O'Reilly, Focused ultrasound-induced blood–spinal cord barrier opening using short-burst phase-keying exposures in rats: a parameter study, Ultrasound Med. Biol. 47 (7) (2021) 1747–1760.

[82] D.E. Goertz, N. de Jong, A.F. van der Steen, Attenuation and size distribution measurements of Definity™ and manipulated Definity™ populations, Ultrasound Med. Biol. 33 (9) (2007) 1376–1388.

[83] C. Pellow, C. Acconcia, G. Zheng, D.E. Goertz, Threshold-dependent nonlinear scattering from porphyrin nanobubbles for vascular and extravascular applications, Phys. Med. Biol. 63 (21) (2018), 215001.

[84] J. Sijl, B. Dollet, M. Overvelde, V. Garbin, T. Rozendal, N. De Jong, D. Lohse, M. Versluis, Subharmonic behavior of phospholipid-coated ultrasound contrast agent microbubbles, J. Acoust. Soc. Am. 128 (5) (2010) 3239–3252.

[85] E. Kimmel, B. Krasovitski, A. Hoogi, D. Razansky, D. Adam, Subharmonic response of encapsulated microbubbles: Conditions for existence and amplification, Ultrasound Med. Biol. 33 (11) (2007) 1767–1776.

[86] S. Qin, C.F. Caskey, K.W. Ferrara, Ultrasound contrast microbubbles in imaging and therapy: physical principles and engineering, Phys. Med. Biol., vol. 54, (6), pp. R27-R57, March 21, 2009.

[87] Y. Ho, C. Yeh, Concurrent anti-vascular therapy and chemotherapy in solid tumors using drug-loaded acoustic nanodroplet vaporization, Acta Biomater. 49 (2017) 472–485.

[88] N. Hosseinkhah, D.E. Goertz, K. Hynynen, Microbubbles and blood–brain barrier opening: a numerical study on acoustic emissions and wall stress predictions, IEEE Trans. Biomed. Eng. 62 (5) (2014) 1293–1304.

[89] B. Dollet, P. Marmottant, V. Garbin, Bubble dynamics in soft and biological matter, Annu. Rev. Fluid Mech. 51 (2019) 331–355.

[90] R. M. Jones, L. Deng, K. Leung, D. McMahon, M. A. O'Reilly, K. Hynynen, Three-dimensional transcranial microbubble imaging for guiding volumetric ultrasound-mediated blood-brain barrier opening, Theranostics, vol. 8, (11), pp. 2909-2926, April 16, 2018.

[91] F. Forsberg, W.T. Shi, B. Goldberg, Subharmonic imaging of contrast agents, Ultrasonics 38 (1–8) (2000) 93–98.

[92] S. Paul, A. Katiyar, K. Sarkar, D. Chatterjee, W.T. Shi, F. Forsberg, Material characterization of the encapsulation of an ultrasound contrast microbubble and its subharmonic response: strain-softening interfacial elasticity model, J. Acoust. Soc. Am. 127 (6) (2010) 3846–3857.

[93] A. Prosperetti, A general derivation of the subharmonic threshold for non-linear bubble oscillations, J. Acoust. Soc. Am. 133 (6) (2013) 3719–3726.

[94] C.D. Arvanitis, M. Bazan-Peregrino, B. Rifai, L.W. Seymour, C.C. Coussios, Cavitation-enhanced extravasation for drug delivery, Ultrasound Med. Biol. 37 (11) (2011) 1838–1852.

[95] A. Prosperetti, Nonlinear oscillations of gas bubbles in liquids. Transient solutions and the connection between subharmonic signal and cavitation, J. Acoust. Soc. Am. 57 (4) (1975) 810–821.

[96] P. Marmottant, S. Van Der Meer, M. Emmer, M. Versluis, N. De Jong, S. Hilgenfeldt, D. Lohse, A model for large amplitude oscillations of coated

bubbles accounting for buckling and rupture, J. Acoust. Soc. Am. 118 (6) (2005) 3499–3505.
[97] A. Sojahrood, H. Haghi, T. Porter, R. Karshafian, M. Kolios, Experimental and numerical evidence of intensified non-linearity at the microscale: the lipid coated acoustic bubble, Phys. Fluids 33 (7) (2021), 072006.
[98] K. Johnston, C. Tapia-Siles, B. Gerold, M. Postema, S. Cochran, A. Cuschieri, P. Prentice, Periodic shock-emission from acoustically driven cavitation clouds: a source of the subharmonic signal, Ultrasonics 54 (8) (2014) 2151–2158.
[99] J.H. Song, K. Johansen, P. Prentice, An analysis of the acoustic cavitation noise spectrum: The role of periodic shock waves, J. Acoust. Soc. Am. 140 (4) (2016) 2494–2505.
[100] B. Gerold, I. Rachmilevitch, P. Prentice, Bifurcation of ensemble oscillations and acoustic emissions from early stage cavitation clouds in focused ultrasound, New J. Phys. 15 (3) (2013), 033044.
[101] C.F. Caskey, S. Qin, P.A. Dayton, K. W. Ferrara, Microbubble tunneling in gel phantoms, J. Acoust. Soc. Am., vol. 125, (5), pp. EL183-EL189, 2009.
[102] B.L. Helfield, X. Huo, R. Williams, D.E. Goertz, The effect of preactivation vial temperature on the acoustic properties of DefinityTM, Ultrasound Med. Biol. 38 (7) (2012) 1298–1305.
[103] C. Pellow, M.A. O'Reilly, K. Hynynen, G. Zheng, D.E. Goertz, Simultaneous intravital optical and acoustic monitoring of ultrasound-triggered nanobubble generation and extravasation, Nano Lett. 20 (6) (2020) 4512–4519.
[104] B. Cheng, C. Bing, R. Chopra, The effect of transcranial focused ultrasound target location on the acoustic feedback control performance during blood-brain barrier opening with nanobubbles, Sci. Rep. 9 (1) (2019) 1–10.
[105] C. Fan, Submicron-bubble-enhanced focused ultrasound for blood-brain barrier disruption and improved CNS drug delivery, PLoS One 9 (5) (2014) e96327.
[106] N. Matsuura, E. Koonar, S. Zhu, B. Leung, M. Seo, N. Sivapalan and D. E. Goertz, Inducing antivascular effects in tumors with ultrasound stimulated micron-sized bubbles, in 2015 IEEE International Ultrasonics Symposium (IUS), 2015, pp. 1-4.
[107] A.K.W. Wood, A review of low-intensity ultrasound for cancer therapy, Ultrasound Med. Biol. 41 (4) (2015) 905–928.
[108] C.P. Keravnou, I. De Cock, I. Lentacker, M. Izamis, M.A. Averkiou, Microvascular injury and perfusion changes induced by ultrasound and microbubbles in a machine-perfused pig liver, Ultrasound Med. Biol. 42 (11) (2016) 2676–2686.
[109] P.T. Yemane, A.K. Åslund, S. Snipstad, A. Bjørkøy, K. Grendstad, S. Berg, Y. Mørch, S.H. Torp, R. Hansen, C. de Lange Davies, Effect of ultrasound on the vasculature and extravasation of nanoscale particles imaged in real time, Ultrasound Med. Biol. 45 (11) (2019) 3028–3041.
[110] H. Chen, A.A. Brayman, A.P. Evan, T.J. Matula, Preliminary observations on the spatial correlation between short-burst microbubble oscillations and vascular bioeffects, Ultrasound Med. Biol. 38 (12) (2012) 2151–2162.
[111] J. Hua, P. Liu, T. Kim, M. Donahue, S. Rane, J.J. Chen, Q. Qin, S. Kim, MRI techniques to measure arterial and venous cerebral blood volume, Neuroimage 187 (2019) 17–31.
[112] V. Daeichin, J.G. Bosch, A. Needles, F.S. Foster, A. van der Steen, N. de Jong, Subharmonic, non-linear fundamental and ultraharmonic imaging of microbubble contrast at high frequencies, Ultrasound Med. Biol. 41 (2) (2015) 486–497.
[113] K. Christensen-Jeffries, O. Couture, P.A. Dayton, Y.C. Eldar, K. Hynynen, F. Kiessling, M. O'Reilly, G.F. Pinton, G. Schmitz, M. Tang, Super-resolution ultrasound imaging, Ultrasound Med. Biol. 46 (4) (2020) 865–891.
[114] F. Foroozan, M.A. O'Reilly, K. Hynynen, Microbubble localization for three-dimensional superresolution ultrasound imaging using curve fitting and deconvolution methods, IEEE Trans. Biomed. Eng. 65 (12) (2018) 2692–2703.
[115] M.A. O'Reilly, K. Hynynen, A super-resolution ultrasound method for brain vascular mapping, Med. Phys. 40 (11) (2013), 110701.
[116] N. Kudo, T. Miyaoka, K. Okada, K. Yamamoto, K. Niwa, Study on mechanism of cell damage caused by microbubbles exposed to ultrasound, in 2002 IEEE Ultrasonics Symposium, 2002. Proceedings. 2002, pp. 1383-1386.
[117] V. Garbin, D. Cojoc, E. Ferrari, E. Di Fabrizio, M. Overvelde, S. Van Der Meer, N. De Jong, D. Lohse, M. Versluis, Changes in microbubble dynamics near a boundary revealed by combined optical micromanipulation and high-speed imaging, Appl. Phys. Lett. 90 (11) (2007), 114103.
[118] B.L. Helfield, B.Y. Leung, D.E. Goertz, The effect of boundary proximity on the response of individual ultrasound contrast agent microbubbles, Phys. Med. Biol. 59 (7) (2014) 1721.
[119] C. Acconcia, B.Y. Leung, A. Manjunath, D.E. Goertz, Interactions between individual ultrasound-stimulated microbubbles and fibrin clots, Ultrasound Med. Biol. 40 (9) (2014) 2134–2150.
[120] X. Chen, J. Wang, M. Versluis, N. de Jong, F.S. Villanueva, Ultra-fast bright field and fluorescence imaging of the dynamics of micrometer-sized objects, Rev. Sci. Instrum. 84 (6) (2013), 063701.
[121] E. Talu, R.L. Powell, M.L. Longo, P.A. Dayton, Needle size and injection rate impact microbubble contrast agent population, Ultrasound Med. Biol. 34 (7) (2008) 1182–1185.
[122] C.A. Sennoga, V. Mahue, J. Loughran, J. Casey, J.M. Seddon, M. Tang, R. J. Eckersley, On sizing and counting of microbubbles using optical microscopy, Ultrasound Med. Biol. 36 (12) (2010) 2093–2096.